



# A Review on Doped/Composite Bismuth Chalcogenide Compounds for Thermoelectric Device Applications: Various Synthesis Techniques and Challenges

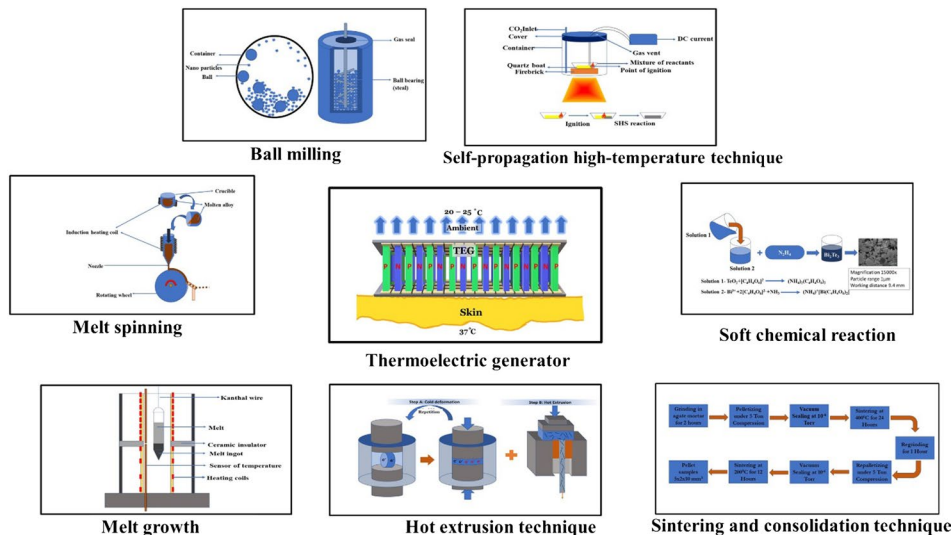
Ganesh Shridhar Hegde<sup>1</sup> · A. N. Prabhu<sup>1</sup>

Received: 27 November 2021 / Accepted: 9 February 2022 / Published online: 14 March 2022  
© The Author(s) 2022

## Abstract

One of the global demands of primary research objectives is to achieve human energy harvesting and self-powered wearable technologies. Bismuth chalcogenides are the trending materials for thermoelectric generators and Peltier coolers due to their notable thermoelectric figure of merit in the low- and room-temperature range. Systematic alloying of bismuth chalcogenides leads to a substantial change in their electrical and thermal transport properties. The high thermoelectric figure of merit ( $ZT$ ) observed in bismuth chalcogenides is due to the rhombohedral crystal structure, lower effective mass, low thermal conductivity, and large band degeneracy. This review is aimed at identifying and quantifying different techniques for effectively improving the thermoelectric properties of doped/composite bismuth chalcogenide compounds. The review also examines the various synthesis methods including ball milling (BM), spark plasma sintering (SPS), self-propagating high-temperature synthesis (SHS), soft chemical reaction, hydrothermal reaction, melt growth (MG), melt spinning (MS), sintering and consolidated synthesis, and hot extrusion, with their respective figures of merit. Since device modification is a challenging task, this report reviews the present research on bismuth chalcogenide alloys to benchmark future development using various techniques.

## Graphical Abstract



**Keywords** Chalcogenide · doping · composite · synthesis technique · thermoelectric properties · thermoelectric wearables

✉ A. N. Prabhu  
ashwatha.prabhu@manipal.edu

Extended author information available on the last page of the article

## Introduction

Thermoelectric materials have attracted global research interest due to their application in energy conversion from heat to electricity.<sup>1</sup> Thermoelectric technology is effectively applied in commercial thermoelectric coolers and stabilizers.<sup>2,3</sup> During the last two decades, attention has been given to thermoelectric technology, mostly due to the increased demand for energy harvesting through waste heat. Thermoelectric materials are assessed by the dimensionless quantity called the figure of merit  $ZT = \frac{S^2\sigma}{K}T$  where  $S$  is the Seebeck coefficient,  $K$  is the thermal conductivity,  $\sigma$  is the electrical conductivity, and  $T$  is the applied temperature. Researchers have been working over the past five decades to increase the thermoelectric figure of merit. Recently, Joseph et al. and Zhang et al. succeeded in improving the  $ZT$  value above unity.<sup>4,5</sup> There are a few compounds that have a high thermoelectric figure of merit, such as skutterudites,<sup>6,7</sup> half-Heuslers,<sup>8,9</sup> clathrates,<sup>10,11</sup> selenides,<sup>12–16</sup> and lead-based compounds.<sup>17–19</sup> It has been observed that material processing plays an essential role in enhancing the thermoelectric figure of merit.

Bismuth telluride and bismuth selenides are found to be functional thermoelectric materials for low- and near-room-temperature applications because of their low thermal conductivity and high weighted mobility. The performance of these materials is also influenced by the minority carriers.<sup>20</sup> Alloys of  $\text{Sb}_2\text{Te}_3/\text{In}_2\text{Te}_3/\text{In}_2\text{Se}_3$  decrease the bipolar effect by increasing the band gap. Both electrons and holes are excited by filling the conduction band and valence bands close to the Fermi level for a particular bandgap. This implies that more heat is absorbed near the hot end and more heat is released near the cold end because of electron–hole recombination, resulting in high thermal conductivity, which negatively impacts the  $ZT$  and the power factor.<sup>21</sup> In addition, the transport properties of bismuth chalcogenides need to be considered.<sup>22–25</sup> High-frequency phonon scattering is significantly responsible for lowering thermal conductivity by introducing mass contrast and bonding variations.<sup>26,27</sup> The presence of density barriers in the material creates selective charge scattering and causes charge mobility variation. In this situation, a few mobility charges are suppressed, and they move to the onset of mixed conduction, resulting in the enhancement of  $ZT$  values.<sup>28</sup> These details must be considered when introducing any foreign elements/composite into the matrix of  $\text{Bi}_2\text{Te}_3$  and  $\text{Bi}_2\text{Se}_3$ .<sup>29</sup> The valence band structure for binary compounds of chalcogenides bismuth selenide and telluride is similar except for the differences in their valence band maxima.<sup>30</sup> In chalcogenides, there is a crossing over of band edges in order to increase thermopower.

The thermoelectric properties of chalcogenides can also be engineered by tuning the microstructure and surface

morphological features. Since  $\text{Bi}_2\text{Se}_3/\text{Te}_3$  is bonded with van der Waals forces between layers, there is a need for substitution on Bi sites by suitable dopants like In/Sb/Sn/Ge, which leads to two quintuple layers of  $\text{Bi}_2\text{Te}_3/\text{Se}_3$  and  $\text{InTe}/\text{Sb}_2\text{Te}_3/\text{GeTe}/\text{SnTe}$ .<sup>31</sup> The insertion of In/Sn/Sb yields an extra electron to the  $\text{Bi}_2\text{Se}_3/\text{Te}_3$  lattice, in which an enhancement in the carrier concentration is noticeable.<sup>32,33</sup> The impact of dopants leads to a narrow peak in the electronic density of states, at the top of the valence band or at the bottom of the conduction band. The dopants also act as an acceptor or donor impurity and pin the Fermi level to the conduction band by creating the delocalized charge carriers which resonate between the band and impurity states.<sup>34</sup> It is observed that phonon scattering is dominant at low carrier concentrations and low temperatures, which reduces thermal conductivity. However, at higher doping concentrations (alloying), the phonon scattering rates increase by point defects, contributing substantially to the reduction in thermal conductivity, except for phonons with fewer frequencies.<sup>35</sup> The replacement of In/Sb/Sn on Bi promotes the formation of antisite defects of  $\text{Bi}_2\text{Se}_3/\text{Te}_3$ .<sup>36–38</sup> The challenging task is to reduce thermal conductivity without weakening the electrical conductivity, which inspires us to review different methods and processing techniques for the synthesis of bismuth chalcogenides.

The embedded thermoelectric generator (TEG) can be optimized on the device and system levels to safeguard the working of a heat harvesting system. Human skin is a multilayer structure containing fat, dermis, and epidermis. Heat interchange occurs through the skin surface due to convection, radiation, evaporation, and blood perfusion. The thermal resistance of the skin is highly reliant on the contact pressure, and skin features such as the surface of human skin are soft but intrinsically rough. Hence the effect of thermal contact resistance at the interface of the skin and TEG on the performance of the wearable thermoelectric device is very significant.<sup>39,40</sup> The materials should have high thermopower for the efficient operation of a boost converter.<sup>41</sup> The surrounding air velocity and ambient temperature affect the power produced by the TEG. The temperature of the core part of the body is usually independent of ambient temperature due to the physiological thermoregulatory system. Hence, the skin's surface temperature is considered the ambient temperature and does not significantly change the environment.<sup>42</sup> With an increase in ambient temperature, the temperature gradient of the TEG decreases, whereas in a warm climate, the ambient temperature rises more than the surface body temperature by the production of power. When the temperature gradient is precisely equal to the skin temperature, the TEG does not generate any temperature difference between the two junctions, with the saturation of rejected heat in an extremely high-velocity air condition.<sup>42,43</sup> The performance of the wearable TEG is affected

by the free air velocity cooling on the cold side. Usually, skin temperature of 28°C to 33°C is applied to the bottom of the metal sheet, while the ambient temperature remains at 23°C. Natural air convection is used on the top of the heat sink. Then, the TEG has the highest temperature gradient and power due to the skin contact. The body gradually heats the TEG and the heat sink until the system reaches a steady state.<sup>44</sup> It is worth knowing that other environmental effects such as humidity and air pressure can also affect the TEG performance. If a TEG has a minimal number of legs, the energy conversion is low because the load resistance is insufficient to obtain a sufficiently high voltage. Inversely, if a TEG has a more significant number of legs, the complete equivalent resistance of the TEG increases, and relatively high Joule losses occur in the TEG. Besides, thermopower is directly proportional to the output voltage. This condition is very important for increasing energy conversion. Hence, the voltage output cannot be improved by having a more significant number of TE elements even if the material's thermopower is small.<sup>45</sup>

So far, many processes have been employed to prepare thermoelectric compounds. Therefore, a timely review is needed of the different methods and their effect on thermoelectric materials. Few review articles are available summarizing the present status of the research on thermoelectric materials.<sup>46</sup> Hence, in this review article, the emerging techniques with description of the working principles are reviewed, and an attempt is made to link the methods, microstructure, and respective thermoelectric properties of doped/composite bismuth chalcogenides. The aspect of the physiology of the human body involved in the production of heat is elaborated. The effects of various parameters on the function of TEGs are reviewed at the material, device, and system levels.

## Electronic Structure

Bismuth telluride is an excellent thermoelectric material due to its complex electronic structure, and it has been widely investigated both theoretically and experimentally. The simple valence rules and spin-orbit interactions complicate the band structure, providing exceptional thermoelectric performance for the material. The qualitative performance of  $\text{Bi}_2\text{Te}_3$  is governed by the p-states of valence interactions within a quintuple layer.  $\text{Te}^{(1)}$  atomic layers between non-bonding adjacent quintuple layers donate to the top of the valence band through van der Waals interactions. Unfilled anti-bonding p-states of bismuth are bonded with tellurium. Two anti-bonding and two bonding sites between Bi and Te atoms of polar bonding are the reason for the positively charged behavior of bismuth. The band structure connects the valence and conduction bands to form a Dirac cone at the

surface. The applied electric field produces the spin-polarized current. By monitoring the Fermi level, the magnitude and spin polarization of the current magnitude and direction can be controlled.<sup>47</sup>

In some cases, bismuth telluride is considered a cubic structure that is viewed along the (111) axis. This can be visualized by linking the atoms to their closest neighbors in the planes below and above in units of five plane values which are near 90° within a few degrees in bismuth.<sup>48</sup> Based on the molecular orbital structure, there is an interaction between  $\text{Te}^{(1)}-\text{Te}^{(1)}$ . It is observed that the band gap has no contribution on  $\text{Te}^{(2)}$ , which deals with the difference in the shape of the lower p orbital in  $\text{Te}^{(1)}$  and  $\text{Te}^{(2)}$  with limited densities of states in the fitted binding model. Covalent bonding is preferred between Te and Bi using a full tight-binding model. A schematic diagram of the electronic band structure is shown in Fig. 1.<sup>49</sup>

Bismuth telluride and bismuth selenide have drawn attention as a practical material in applications such as conventional thermoelectric systems. The  $\text{Bi}_2\text{Te}_3/\text{Se}_3$  crystal structure is a rhombohedral tetradymite type with space group  $R\bar{3}m$  and is defined by a hexagonal unit cell, as shown in Fig. 2a and b. The Te/Se unit cell comprises five covalently bonded monatomic sheets along the *c*-axis in the sequence  $-\text{Te}/\text{Se}_{(1)}-\text{Bi}-\text{Te}/\text{Se}_{(2)}-\text{Bi}-\text{Te}/\text{Se}_{(1)}-\text{Bi}-\text{Te}/\text{Se}_{(2)}-\text{Bi}-\text{Te}_{(2)}/\text{Se}_{(2)}-\text{Bi}-\text{Te}_{(1)}/\text{Se}_{(1)}$ . Due to this crystal structure, the lattice constant of the *c*-axis is approximately seven times as large as that of the *a* and *b* axes, leading to remarkable anisotropic behavior.

In bismuth-, tellurium-, antimony-, and indium-doped alloys, negatively charged antisite defects such as  $\text{Sb}_{\text{Te}}$ ,  $\text{Bi}_{\text{Te}}$  and  $\text{In}_{\text{Te}}$  are created when there is excess cation occupancy on empty anion sites, which prefer p-type conductivity between compounds.<sup>50,51</sup> Anion vacancies  $V_{\text{Te}}^{\cdot\cdot}$  and  $V_{\text{Se}}^{\cdot\cdot}$  accompanying positive charges are produced when the vacant anion sites are retained and are satisfied by the electrons. The antisite defect concentration of solid solutions is dependent on composition and doping, where more minor differences in atomic radii and electronegativity are present between cations and anions.<sup>52</sup>

## Various Synthesis Techniques

The synthesis process has a vital role in obtaining the desired thermoelectric materials (TEM). The past two decades have witnessed the emergence of different techniques for preparing thermoelectric compounds. Cost-effective and straightforward strategies such as solid-state reaction and melting still play a vital role in producing high-performance TEMs. In addition, there are a few progressive preparation techniques including high-energy ball milling and mechanical alloying to obtain TEMs

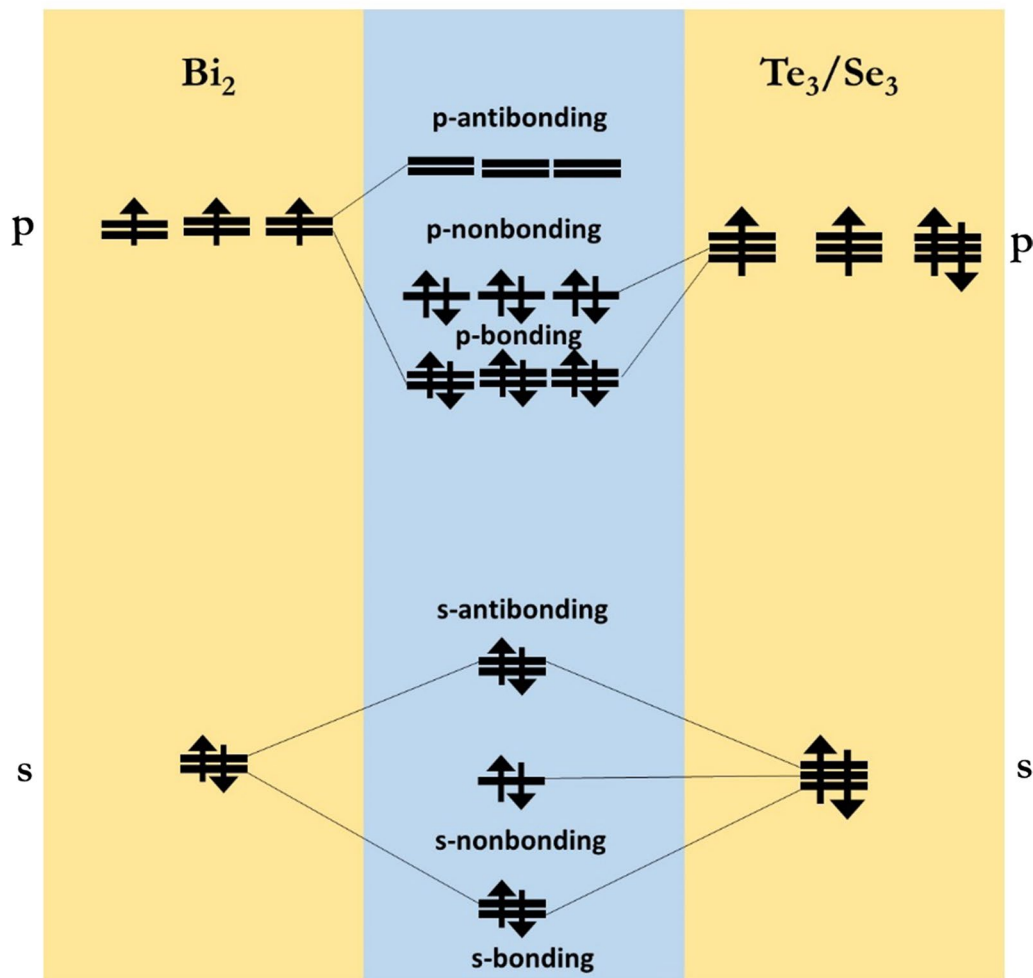


**Fig. 1** Energy level diagram of  $\text{Bi}_2\text{Te}_3/\text{Se}_3$ .

in powder in bulk form.<sup>53</sup> Chemical synthesis methods like hydrothermal and solvothermal techniques are used around the globe to control the morphology, dimensions, and size of the materials.<sup>54</sup> Synthesis by grinding and sintering plays an active role in preparing bulk TEM. In melting and casting methods, the compounds are deliberately crushed and sintered again to regulate the grain size, particle size, lattice parameters, and strain.<sup>55</sup> For layered compounds like  $\text{Bi}_2\text{Te}_3$ ,  $\text{Bi}_2\text{Se}_3$ ,  $\text{InTe}$ ,  $\text{InSe}$ , etc., melting/zone melting techniques are utilized because these techniques are useful in purifying the phase of the compounds.<sup>56</sup>

In the present section, we mainly emphasize the emerging methods of producing nanostructure/polycrystalline TEMs and their operating principles with respect to their structural, morphological, and thermoelectric properties.

### Ball Milling (BM)

Ball milling is one of the most widely used pulverizing techniques and can be applied as mechanical alloying (MA) and mechanical grinding (MG). MA can be used to synthesize compounds from elemental powders by a mechanochemical effect.<sup>57,58</sup> The collision energy between the balls is successfully relocated to milled powders to conduct the reaction in a dry milling form.<sup>59</sup> Mixing mills, planetary ball mills, and shakers are the various BM machines, although the operating principles for each instrument are similar. The main purpose of using BM is to synthesize the compounds to obtain micro-grains or nanostructured powders and to combine composites.<sup>60,61</sup> The ratio of large balls to small balls, BM speed, time, and number of balls can be adjusted to obtain the optimized intensity of pulverizing. In addition,

fracturing and cold welding in high-energy ball mills leads to further grinding.<sup>62</sup> Excessive cold welding is resisted by steric acid when ductile powders are crushed. The refined structure increases the scattering of phonons in order to decrease thermal conductivity. Using BM combined with a subsequent hot-press technique, Poudel et al. obtained a  $ZT$  value of 1.4 at 400 K for BiSbTe nanocrystals. The bipolar effect was reduced by the existence of an interfacial potential that scattered more electrons than holes.<sup>63</sup>

On the other hand, BM also exhibits a remarkable effect on the electrical transport properties of compounds due to the impedance of carrier transport in nanostructures.<sup>64</sup>

Charge density is exaggerated when charge point defects are introduced into alloys based on chalcogenides such as bismuth telluride and bismuth selenide and using Sb, In, Sn dopants.<sup>65–67</sup>  $\text{Bi}_2\text{Te}_3$  is usually a p-type material because of antisite defects which are negatively charged, and it changes to an n-type material due to a higher number of donor-like effects and anion vacancies.<sup>65–69</sup> A comparison of the thermoelectric performance of ingots and bulks of spark plasma sintered (SPS) pellets (BM + SPS) of n-type BiTeSe and p-type BiSbTe was reported by Hue et al.<sup>70</sup> As noted by Liu et al.,<sup>71</sup> the free charge density of BiTeSe has five times more scattering than p-type BiSbTe with the evaporation of

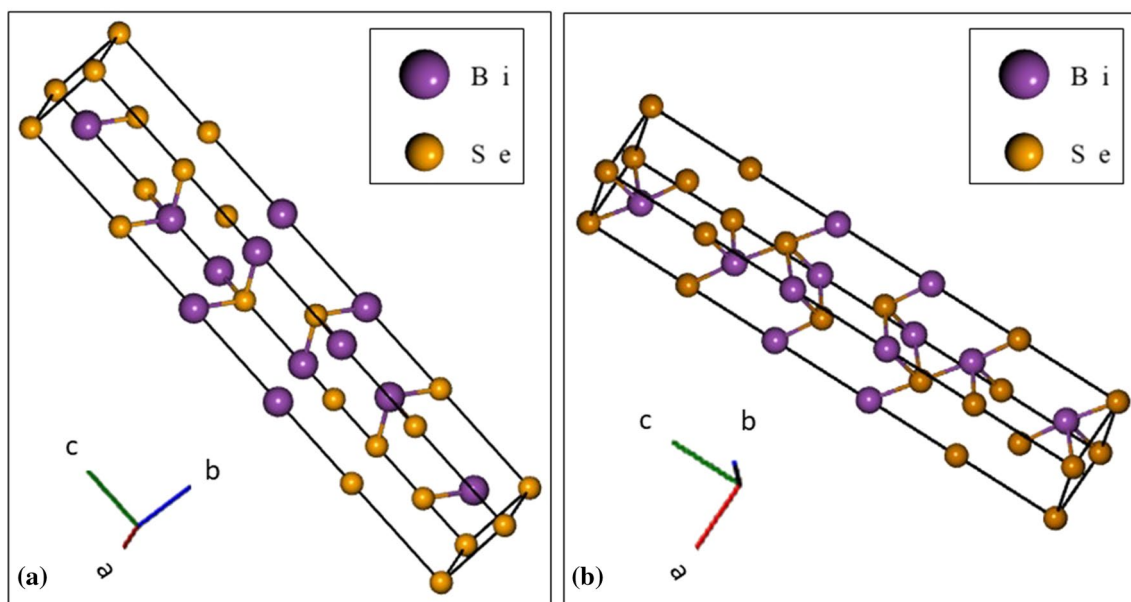


**Fig. 2** (a) Schematic diagram of  $\text{Bi}_2\text{Se}_3$  crystal structure (CIF id: mp-342022). (b) Schematic diagram of  $\text{Bi}_2\text{Te}_3$  crystal structure (CIF id: mp-541837) (images generated by the software BURAI Quantum ESPRESSO).

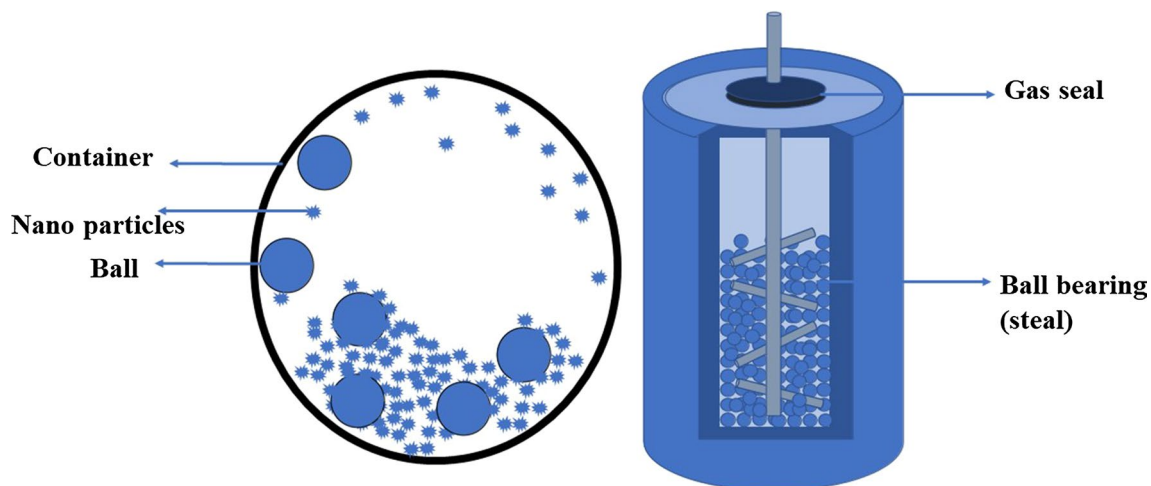


**Fig. 3** Schematic of ball milling bismuth chalcogenide.

Te ions. A schematic diagram of ball milling is shown in Fig. 3. BiTeSe has much less reproducibility under the BM process.<sup>72,73</sup> Some of BM-synthesized materials are reported in Table I.

### Self-Propagating High-Temperature Synthesis (SHS)

Self-propagating high-temperature synthesis is an analogous auto wave procedure for the propagation of combustion movement introduced by point heating a sample's minor portion.<sup>74,75</sup> The chemical reaction is contained in the combustion region, which impulsively proliferates on a chemical dynamic medium. The materials are purified by maintaining the stoichiometric ratio as the combustion wave permits over the sample.<sup>76,77</sup> The current procedure

can be adapted mainly for inorganic materials such as bismuth, indium, tellurium, and selenium.<sup>78–80</sup>

SHS synthesis offers advantages including a one-step process, scalable nature, and maintenance of stoichiometry, making some of the thermoelectric materials very popular.<sup>74,81</sup> In the SHS process between binary reactants, the combustion reaction continues in the mode of diffusion, and the reaction rate is partly through the second reactant diffusion. The nano-sized products are obtained from nanoscopic reactants, providing in situ nanostructures in the resultant thermoelectric materials.<sup>75</sup> These nano-sized materials are influenced by mechanical action. As there is an increase in reactant reactivity, there is a corresponding increase in defect concentration which significantly induces automatic activation of reactants; however, the controlled propagation process wave is a vital task.<sup>82</sup> A

**Table I** *ZT* values of some reported bismuth chalcogenide-based compounds prepared by various synthesis techniques

Sl. no.	Compound	Technique	Thermoelectric figure of merit ( <i>ZT</i> )	Temperature (K)
1	Bi <sub>2</sub> Te <sub>3</sub> +SiC	Ball milling	0.65	450 <sup>108</sup>
2	Bi <sub>2</sub> Te <sub>3-x</sub> Se <sub>x</sub>	Ball milling	1.29	398 <sup>109</sup>
3	Bi <sub>2</sub> Te <sub>3</sub>	Ball milling	1.0	300 <sup>60</sup>
4	(Bi,Sb) <sub>2</sub> Te <sub>3</sub>	Ball milling	1.0	323 <sup>110</sup>
5	Bi <sub>2</sub> Te <sub>3-x</sub> Se <sub>x</sub>	SHS	0.94	420 <sup>77</sup>
6	Bi <sub>2</sub> Te <sub>3</sub>	SHS	0.39	300 <sup>111</sup>
7	Bi <sub>2</sub> Se <sub>1.5</sub> Te <sub>1.5</sub>	SHS	0.70	500 <sup>112</sup>
8	Bi <sub>2</sub> Te <sub>3</sub>	SHS	0.65	450 <sup>113</sup>
9	Bi-Sb-Te	Soft chemical reaction	1.28	303 <sup>114</sup>
10	Bi <sub>2</sub> Te <sub>3</sub>	Soft chemical reaction	0.70	473 <sup>97</sup>
11	Bi <sub>0.5</sub> Sb <sub>1.5</sub> Te <sub>3</sub> + Sb <sub>2</sub> Te <sub>3</sub>	Soft chemical reaction	0.55	400 <sup>115</sup>
12	Bi <sub>2</sub> Te <sub>3</sub>	Soft chemical reaction	0.54	400 <sup>116</sup>
13	Bi <sub>2</sub> Te <sub>3-x</sub> Se <sub>x</sub>	Soft chemical reaction	0.57	475 <sup>117</sup>
14	(Bi <sub>0.2</sub> Sb <sub>0.8</sub> ) <sub>2</sub> Te <sub>3</sub>	Melt spinning	0.55	300 <sup>118</sup>
15	Bi <sub>2</sub> Te <sub>2.4</sub> Se <sub>0.6</sub>	Melt spinning	1.05	300 <sup>119</sup>
16	Bi <sub>2</sub> Te <sub>2.7</sub> Se <sub>0.3</sub>	Melt spinning	0.84	423 <sup>120</sup>
17	Bi <sub>0.52</sub> Sb <sub>1.48</sub> Te <sub>3</sub>	Melt spinning	1.56	300 <sup>121</sup>
18	Bi <sub>2</sub> (Te,Se) <sub>3</sub>	Melt spinning	1.05	420 <sup>122</sup>
19	Bi <sub>1.5</sub> Sb <sub>0.5</sub> Te <sub>2.7</sub> Se <sub>0.3</sub>	Melt growth	1.05	330 <sup>123</sup>
20	Bi <sub>2</sub> Te <sub>3</sub> -Sb <sub>2</sub> Te <sub>3</sub>	Melt growth	0.03	300 <sup>124</sup>
21	Bi <sub>1.85</sub> In <sub>0.5</sub> Te <sub>2</sub> Se <sub>1</sub>	Melt growth	1.1	300 <sup>67</sup>
22	Bi <sub>0.5</sub> Sb <sub>1.5</sub> Te <sub>3-x</sub> Se <sub>x</sub>	Melt growth	1.1	300 <sup>125</sup>
23	(Bi <sub>0.98</sub> In <sub>0.02</sub> ) <sub>2</sub> Se <sub>2.7</sub> Te <sub>0.3</sub>	Melt growth	0.28	350 <sup>126</sup>
24	(Bi <sub>0.96</sub> Sn <sub>0.04</sub> ) <sub>2</sub> Se <sub>2.7</sub> Te <sub>0.3</sub>	Solid-state reaction and sintering	0.27	300 <sup>127</sup>
25	Bi <sub>2</sub> Te <sub>3</sub>	Sintering	1.6	420 <sup>128</sup>
26	Bi <sub>2-x</sub> Sb <sub>x</sub> Te	Sintering	1.2	360 <sup>129</sup>
27	(Bi <sub>0.98</sub> In <sub>0.02</sub> ) <sub>2</sub> Te <sub>2.7</sub> Se <sub>0.3</sub>	Solid-state reaction and sintering	0.67	350 <sup>50</sup>
28	(Bi <sub>0.98</sub> In <sub>0.02</sub> ) <sub>2</sub> Se <sub>2.7</sub> Te <sub>0.3</sub>	Solid-state reaction sintering	0.023	350 <sup>51</sup>
29	Bi <sub>2</sub> Te <sub>2.7</sub> Se <sub>0.3</sub>	Hot extrusion	0.9	300 <sup>130</sup>
30	Bi <sub>2</sub> Te <sub>2.7</sub> Se <sub>0.3</sub>	Hot extrusion	0.9	300 <sup>131</sup>
31	Bi <sub>2</sub> Te <sub>2.7</sub> Se <sub>0.3</sub> +SbI <sub>3</sub>	Hot extrusion	0.96	300 <sup>132</sup>

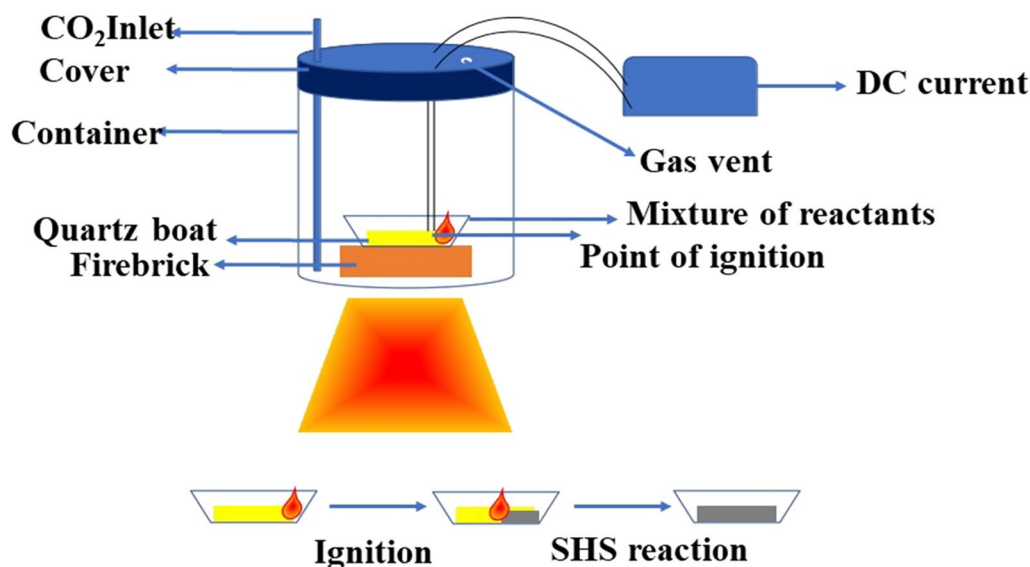


**Fig. 4** Basic schematic representation of self-propagating high-temperature technique.

schematic representation of the SHS technique is provided in Fig. 4.

### Soft Chemical Reaction (Wet Chemical Process)

In some nanostructured thermoelectric compounds, the controlled surface morphology is achieved by wet chemical processes, including the sol–gel technique, solvothermal synthesis, and microwave synthesis. The pros and cons of the solution-based synthesis process are discussed in this section. The precursor of ingredients is combined in superior templates in a stoichiometric ratio of an aqueous solution. The solution is inserted into a closed autoclave with chosen heating temperature followed by cooling to room temperature. The autoclave strictly controls the pH value, pressure, and additive concentration. It is noted that the morphology and grain size can be altered through the peripheral condition. Zhao et al.<sup>83</sup> reported  $\text{Bi}_2\text{Te}_3$  nanotubes having diameters less than 100 nm by performing hydrothermal synthesis. Many reports are available on this technique, in which  $\text{BiCl}_3$  and  $\text{TeO}_2$  are used as initial precursors.<sup>84–89</sup> To reduce toxicity, Muramatsu et al.<sup>90</sup> applied green hydrothermal solution synthesis using ascorbic acid in an aqueous solution as a reducing agent.

Microwave synthesis (MWS) has been used consistently for the large-scale one-pot preparation of thermoelectric materials.<sup>91–93</sup> Although solvothermal synthesis was established with regulation over the surface morphology and size of the particle, it has been observed that sintering is a fairly difficult task because of low density and an increase in the secondary phase of compounds. Industrialization of the MWS method was performed by Li et al.<sup>94</sup> for a SnTe

compound by varying the sizes from micro- to nanoscale using a period of 20 min, which enhanced the  $ZT$  by 2.3 times over that of the powder synthesis method. However, there are some unavoidable experimental constraints for the MWS method: (i) requirement of practical experiments on applicable parameters; (ii) superheating, speculation of hotspots, and the hot surface of nonthermal effect caused due to the extreme measurement of reaction pressure and temperature; and (iii) some of the complex system synthesis was found to be a tough task in the MWS technique for developing and designing thermoelectric nanostructures.<sup>95,96</sup> Some of the available thermoelectric materials prepared by solvothermal method are mentioned in Table I. Figure 5 shows a schematic representation of soft chemical reaction synthesis technique.

### Melt Spinning (MS)

Melt spinning is a beneficial technique for quick molten solution cooling. A molten alloy thin stream is poured on a spinning wheel.<sup>97–99</sup> The melting heat is quickly transferred to the wheel followed by rotation, which sustains the amorphization of liquid continuously, producing thin tapes and ribbons.<sup>100</sup> The local cooling and cooling rate regulate the microstructure of the materials in the synthesis process and are maintained through processing parameters in melt spinning.<sup>101</sup> Lee et al. showed that ribbons can be made thin monotonically by increasing the wheel's speed and cooling rate. Si-Ge-Au showed a  $ZT$  of 2 at 300 K when prepared by the MS method.<sup>89</sup> Dey et al.<sup>102</sup> observed a  $ZT$  of 0.14 for BiSbTe at 350 K. The unique nanostructure and microstructure produced in the melt spinning process

led to enhanced thermoelectric performance. Low-dimensional structures of an amorphous nature with 5–15-nm nano-crystallites with coherent interfaces were observed. These interfaces were supposed to be the center of strong phonon scattering zones, which deliver the route for conduction of charges, which is beneficial for thermoelectric performance.<sup>103</sup> A schematic diagram of melt spinning is represented in Fig. 6. Thermoelectric figure of merit values of some reported materials are given in Table I.

### Melt Growth (MG)

One of the rich conventional methods for preparing single-crystal thermoelectric materials is the melt growth (MG) technique. Melting is a unidirectional solidification procedure applied for materials like  $\text{Bi}_2\text{Te}_3$ ,  $\text{Bi}_2\text{Se}_3$  in industries.<sup>104</sup> In laboratories, chalcogenide compounds are taken in a quartz tube sealed in a vacuum of  $1.333 \times 10^{-7}$  kPa, and the temperature profile is prearranged in a crystal puller. With the help of a programmed thermal profile,

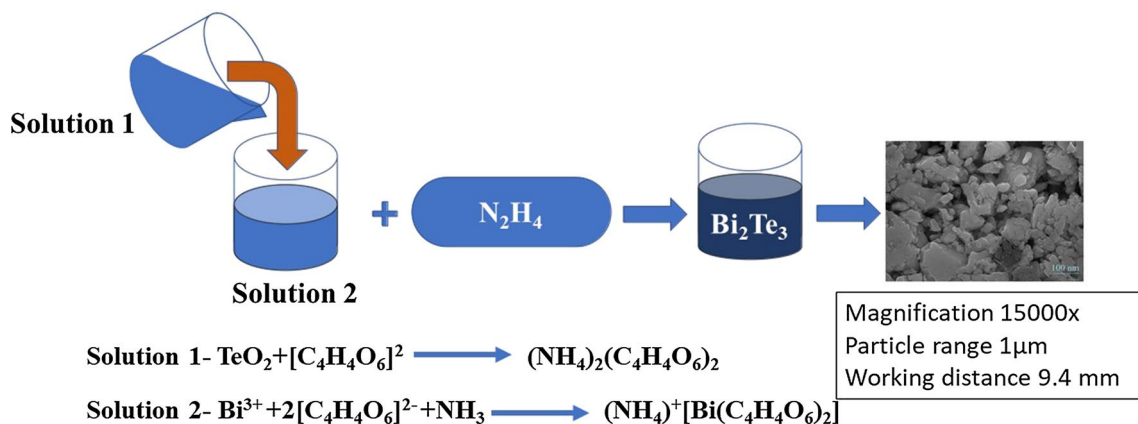


Fig. 5 Schematic representation of soft chemical reaction of bismuth telluride synthesis.

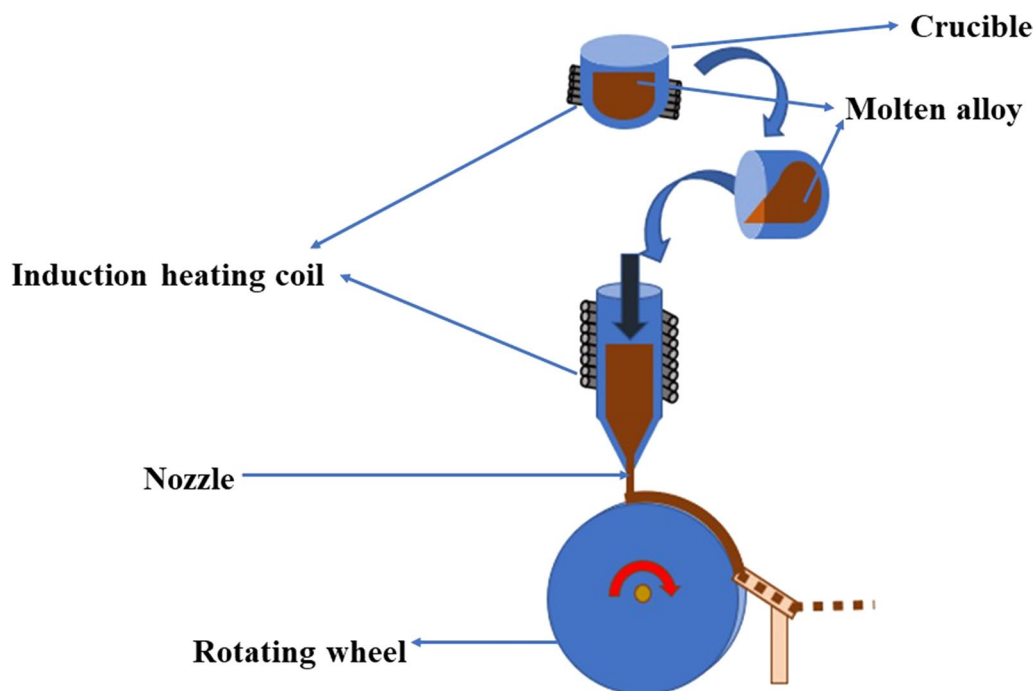


Fig. 6 Schematic representation of melt spinning technique.



the compound is liquefied in the crystal puller furnace. The cooling is done very slowly at a specific rate ( $2^{\circ}/3^{\circ}$  per min), and the pulling is also done simultaneously. The ampoule holding a grown ingot of a single crystal (25 mm) is taken out of the furnace, separated from the ampoule, and cut into anticipated dimensions for measurements and characterization. In some specific systems, post-treatment, the cooling rate is optimized for growing a single crystal ingot to regulate the size and morphology of single crystals.

The melt growth technique can be classified based on heating source, including arc, eddy current, and electrical resistance such as arc melting, induction melting, levitation melting, and Bridgeman technique. Figure 7 shows the schematic diagram of the melt growth technique. Some of the reported compounds prepared from the melt growth technique are given in Table I.

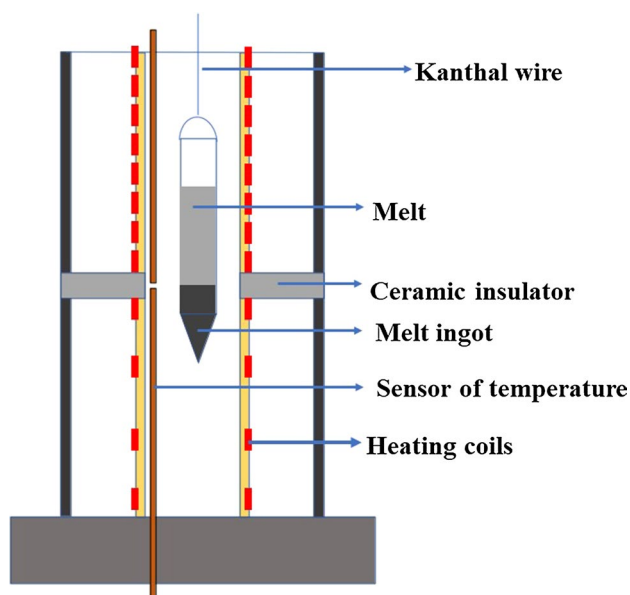


Fig. 7 Schematic representation of melt growth technique.

## Sintering and Consolidated Synthesis

A proper sintering process can attain a compaction of crystallite size and stabilization of the primary phase under appropriate conditions. The compressed samples have better crystallinity and specific shape and are used for characterization and measurements. Sintering is the process that precedes the fabrication of bulk compounds. Various special positive effects on the thermoelectric properties of the materials can be gained through hot pressing (HP) and spark plasma sintering (SPS).<sup>105</sup>

Over the past decade, SPS has brought a nanostructure dimension to the polycrystalline bulk materials. In SPS, a die with loaded powder is sandwiched between two punches and positioned in displaced graphite plates. To achieve an excellent electrical connection, the punch and the powder are inserted by graphite papers.<sup>104–106</sup> By applying direct current at low voltage and high current (1–10 kA), at the rate of  $1000^{\circ}\text{C min}^{-1}$ , Joule heat is generated with uniaxial pressure loaded to enable compression. Hence, the inherited nanostructures are manufactured using a reduced ingot and refined grains of powder to obtain better performance of thermoelectric materials with less thermal conductivity.<sup>95,107</sup> Some of the reported thermoelectric materials are given in Table I. The steps involved in the sintering technique are shown in Fig. 8.

## Hot Extrusion Method

High-purity precursors like Bi, Te, and Se are weighed stoichiometrically. The powder is manufactured by high-frequency introduction under an argon atmosphere in a graphite crucible at a temperature of  $200^{\circ}\text{C}$ .  $\text{N}_2$  gas is introduced into the chamber operating at a pressure of 1.2 MPa. A conventional mechanical sieving technique measures the size distribution of the powder. To remove the oxygen from the powder surface, atomized gas powder is reduced at  $360^{\circ}\text{C}$  for 4 h. The consolidated alloy powder is compacted using Al alloy for 1 h at  $450^{\circ}\text{C}$ . None of the extruded bars showed

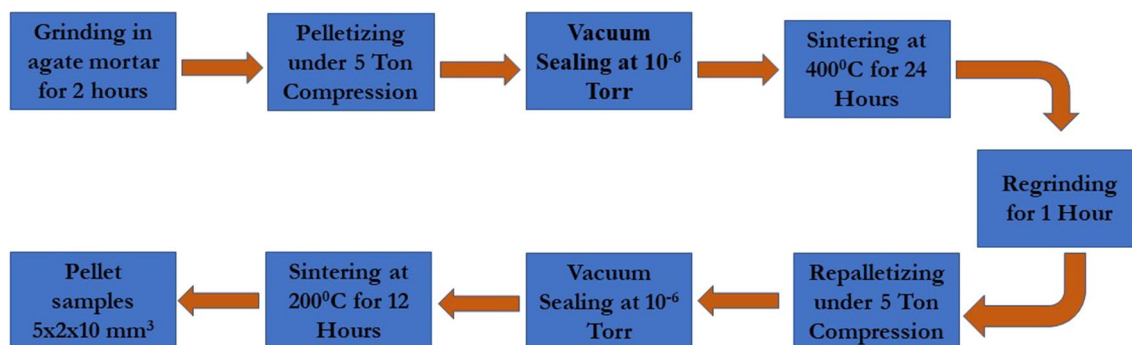
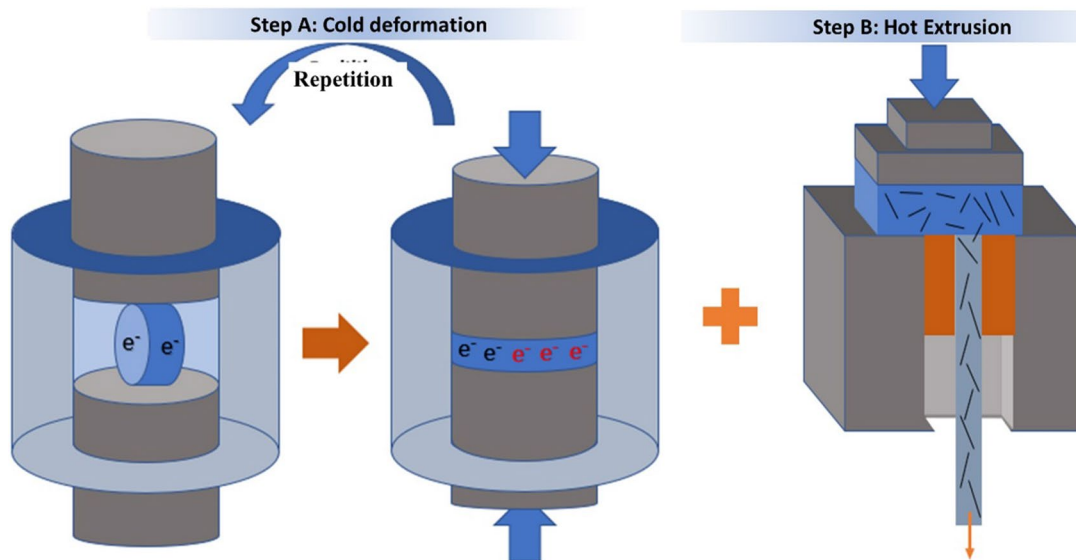


Fig. 8 Steps involved in sintering and consolidation technique.



**Fig. 9** Schematic diagram of the hot extrusion process.

blistering or cracking on the surface. The density of the hot-extruded compounds was measured using the Archimedes principle. A schematic diagram of the hot extrusion process is shown in Fig. 9.

## Crystal Structure

The crystal structure of prepared chalcogenides of bismuth telluride and bismuth selenides are found to crystallize in the tetradymite crystal structure.<sup>133</sup> A rock salt structure is observed between Bi, Te, and Se. The associated valences of  $\text{Bi}^+$  ( $s^2p^0$ ) and  $\text{Te}^{-2}$  are indicated by the differences in the electronegativity among Bi, Te, and Se. Removing the metal layer of every adjacent packed plane forms a rhombohedral structure of tetradymite IV and V semiconductor.<sup>119,134</sup> Quintuple stalk sequences of Te–Bi–Te and Se–Bi–Se are formed in  $\text{Bi}_2\text{Te}_3$  and  $\text{Bi}_2\text{Se}_3$ , respectively. The numbers in parentheses differentiate equivalent Te and Se sites. Bonds between the Te, Se, and Bi are polar covalent bonds, where weak van der Waals bonding exists between  $\text{Te}^{(1)}\text{--Te}^{(1)}$  and  $\text{Se}^{(1)}\text{--Se}^{(1)}$  atoms.<sup>38,135,136</sup> As a result, there is an easy cleavage for the basal planes of a and c directions.

The doping of Se in the site of tellurium does not result in any substantial structural change in the material, but there is a shift to the higher angle  $2\theta$  side with increasing content of Se atoms. This indicates the suitable incorporation of Se into the matrix of  $\text{Bi}_2\text{Te}_3$ . As a result, there is a variation in lattice constant, which was reported by Pan et al..<sup>137</sup> The crystal structure of Sb-doped  $\text{Bi}_2\text{Te}_3$  attained a small particle size with better crystallinity.<sup>138</sup> A significant alteration of the intensity of X-ray diffraction (XRD) patterns

and peak shifting was observed in the hybridized method of BM+SPS.<sup>55</sup> There was no significant deviation in the XRD patterns observed in the SHS method, as the relative density of the sample was greater than 98%, but the crystallinity was poorer than the MG technique.<sup>139</sup> The surface morphology of the compound was found to exhibit a parallel set of cleavage planes consistent with the orientation factor. A change in the lattice parameters of indium- and selenium-doped bismuth telluride was found with an increase in lattice compressive strain.<sup>50,51</sup> No impurity was observed in as-synthesized samples of  $\text{Bi}_2\text{Te}_3$  prepared by rational nanostructure design, as reported by Min et al..<sup>140</sup> Specific reports are available on the thermoelectric properties of ball-milled powder of bismuth antimony telluride, where the single-phase XRD patterns were obtained with a rotation speed of 150 rpm with no impurity peaks.<sup>141</sup>

## Thermoelectric Properties

High semiconducting behavior is required to develop a perfect, optimized thermoelectric material of both p and n type with comparable performance. Yan et al..<sup>142</sup> found that excess electrons introduced into the lattice by deformation led to a donor-like effect. Bi atoms occupying Te sites were diffused back towards the original sublattice, and excess Te vacancies were produced.

The deformation effect was also examined for the compound  $\text{Bi}_2\text{Se}_3\text{--Bi}_2\text{Te}_3$ . It was observed that there is an unusual reduction in the electrical resistivity of cold-pressed samples. But the Seebeck coefficient was found to be within the intrinsic range due to low carrier concentration.

Preparation of the  $\text{Bi}_2\text{Te}_3$ -rich side of  $\text{Bi}_2\text{Te}_3$ – $\text{Bi}_2\text{Se}_3$  via zone melting and the hot-pressing method was investigated by Heon et al. to determine the thermoelectric properties.<sup>143</sup> The zone-melted ingot was found to be affected by the dopant, as the ingot composition is constant, whereas thermoelectric properties of hot-pressed material are related to variation of the carrier concentration caused by the generation of electronically active defects from many sources. When the content of Se was less than 4 wt.%, the highest thermoelectric figure of merit was found to be 0.3.

$\text{Bi}_2\text{Te}_3$ – $\text{Bi}_2\text{Se}_3$ – $\text{Sb}_2\text{Te}_3$  of a quasi-quaternary solid solution form showed a  $ZT$  of 1.1 at 300 K. The composite system has low carrier concentration due to non-ignorable intrinsic excitation. The electrical conductivity and Seebeck coefficients increase with the content of  $\text{Sb}_2\text{Te}_3$ . Because of the suppressed bipolar conduction, there is a decrease in the lattice thermal conductivity in an  $x=0.1$  zone-melted (ZM) ingot compared to an  $x=0$  ZM ingot.<sup>144</sup> An intrinsic point defect-based bismuth telluride compound showed a decrease in electrical conductivity in a low-temperature regime, whereas severe intrinsic excitation in the high-temperature region beyond 350 K caused a turnover of electrical conductivity. It was found that mechanical sintering has a significant impact on the donor-like effect.<sup>40</sup> The p-type chemical composition of  $x=0, 0.05, 0.16, 0.20, 0.25$   $(\text{Bi}_2\text{Te}_3)_x(\text{Sb}_2\text{Te}_3)_{1-x}$  is fabricated by zone melting. The increase in the composition of  $\text{Bi}_2\text{Te}_3$  in Bi–Sb–Te lowers the concentration of holes systematically with the highest  $ZT$ , which was found to be 1.14 at 350 K.<sup>145</sup> High-energy ball milling was carried out for n-type  $\text{Bi}_2\text{Te}_3$  bulk compound followed by spark plasma sintering, which contributed to the uniformity of the grains and grain boundaries in the materials, thus resulting in increased thermoelectric properties with the highest  $ZT$  value of 1.2 at 480 K.<sup>146</sup> The parallel and perpendicular directions of electrical resistivity of the reduced of pretreated powder were found to decrease by 25% and 15%, respectively, as compared to dry powder samples. There was also an enhancement of Seebeck coefficient by 115% at room temperature for reduced pretreated powder in the perpendicular direction compared to dry powder sample, with a  $ZT$  of 0.1 at 500 K.<sup>147</sup>

In order to investigate the effect of graphene nanoparticle structural integrity on the thermoelectric properties,  $\text{Bi}_2\text{Te}_3$ – $\text{Bi}_2\text{Se}_3$ /graphene composites were prepared by Faraha et al.<sup>148</sup> through ball milling and spark plasma sintering techniques. The electrical conductivity of samples with higher graphene concentration was found to be low due to the agglomeration and increased scattering of charge carriers. As the milling time of graphene was increased, the appearance of large defects and low structural integrity was noted, with an improved Seebeck coefficient. The electronic part controlled the thermal conductivity of the samples because of the high electrical conductivity of the optimized samples.

However, a noticeable reduction in the lattice thermal conductivity was observed due to the enhanced scattering at the interfaces. As a result of graphene addition,  $ZT$  was found to increase in the composite samples compared to pristine  $\text{Bi}_2\text{Te}_3$ – $\text{Bi}_2\text{Se}_3$ .  $\text{Bi}_{0.3}\text{Sb}_{1.7}\text{Te}_{3.0}$ , thermoelectric compound was fabricated using an yttrium vessel and stainless steel vessel by Mongkol et al.<sup>149</sup> The mixture milled at 150 rpm with an yttrium vessel was found to have a higher  $ZT$  value than the compound milled in a stainless steel vessel by a factor of 1.7 at 500 K. The electrical conductivity, Seebeck coefficient, and thermal conductivity of the bismuth antimony telluride were  $4.6 \times 10^4$  S/m, 295  $\mu\text{V}/\text{K}$ , and 0.94 W/mK, respectively, at 500 K (Fig. 10a, b, c, and d).

The mechanochemical method of producing nanostructured bismuth antimony telluride with added silicon carbide and alumina nanoparticles was reported by Shyam et al.,<sup>150</sup> which showed a gradual decrease in the Seebeck coefficient from 0.05 mW/K to 0.04 mW/K at around 310° C. In this investigation, (p-type)  $\text{Bi}_{0.3}\text{Sb}_{1.7}\text{Te}_{0.3}$  thermoelectric compounds were synthesized at various ball-milling speeds using yttrium balls. The powder milled at 150 rpm exhibited a single-phase XRD pattern with a sintered temperature of 350°C. The grain size was found to be approximately 1  $\mu\text{m}$  at the fractural surface, and the  $ZT$  of the compound was about 1.0 at 350°C. Another study investigated the preparation and thermoelectric performance of BiSbTe thermoelectric materials fabricated at different ball-milling speeds with yttria-stabilized zirconia ceramic balls and vessels.<sup>151</sup> The study of ruthenium composite revealed a certain mass fraction range and an increase in the content of Ru nanoparticles with local grain refinement. The thermoelectric properties were enhanced by low energy carrier filtering and a wide range of phonon scattering. The investigation also explored optimization of second-phase thermoelectric properties of nanoparticles with  $ZT$  of 0.86 at 420 K.<sup>152</sup> Recently, boron- and indium-doped  $\text{Bi}_{0.48}\text{Sb}_{1.52}\text{Te}_3$  thermoelectric compounds were synthesized through the zone-melting method by Wang et al.<sup>153</sup> The synergistic effects yielded a maximum  $ZT$  of 1.45 at 350 K and a power factor of 41  $\mu\text{W}/\text{Cm K}^2$  in  $\text{Bi}_{0.48}\text{Sb}_{1.51}\text{In}_{0.005}\text{Te}_3 + 0.6$  wt.% boron-doped samples (Fig. 11a, b, c, and d). In our recent research work,<sup>126</sup> a considerable reduction in electrical resistivity was found in  $(\text{Bi}_{0.96}\text{In}_{0.04})_2\text{Se}_{2.7}\text{Te}_{0.3}$ , leading to an increase in the power factor (1900  $\mu\text{W}/\text{mK}^2$ ) and  $ZT$  (0.28) by a factor of about 8.0 and 4.1, respectively, compared to  $\text{Bi}_2\text{Se}_3$  (Fig. 12a, b, c, and d).

Along with the melt growth and ball milling technique, the melt spinning technique has witnessed an influence on the properties of chalcogenide thermoelectric materials.<sup>154</sup> The influence of the density of states and microstructure decomposition of spinodal microscale on water-quenched 0.1 wt.% PbTe was investigated by Jaquat et al.<sup>155</sup> The cooling rate modified fundamental properties like electrical

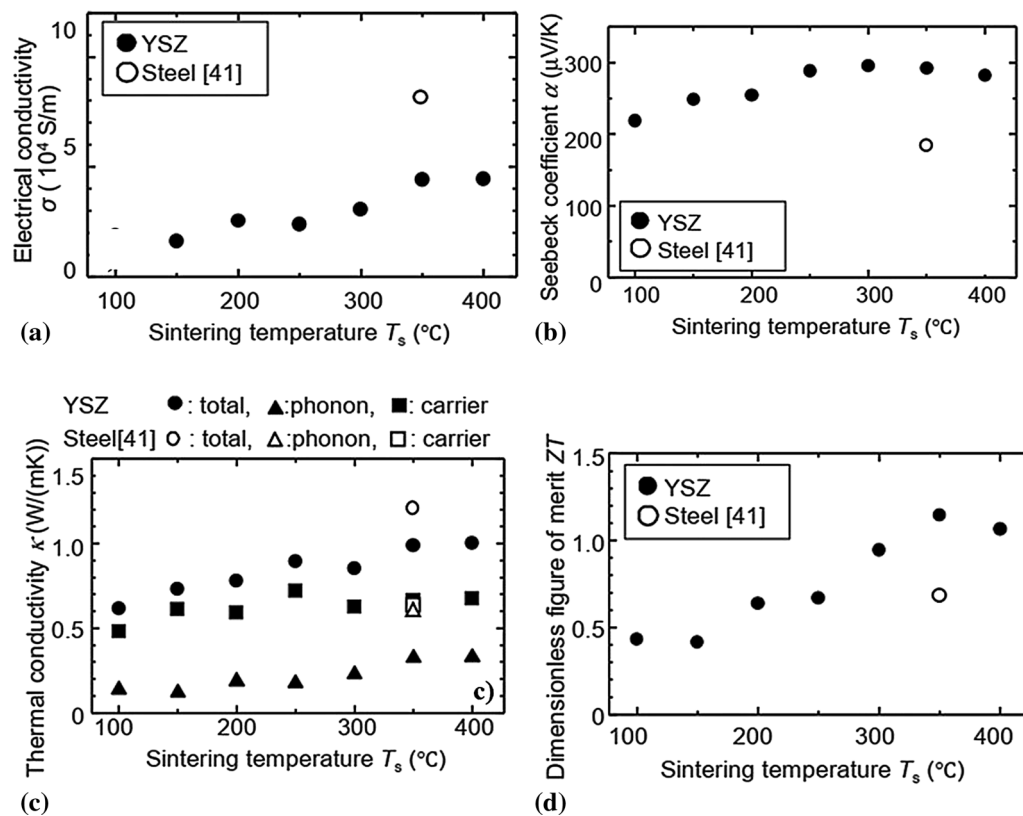


**Fig. 10** Temperature-dependent (a) electrical resistivity, (b) Seebeck coefficient, (c) total thermal conductivity, and (d)  $ZT$  value of bismuth antimony telluride. Reprinted from *Ceramics international*, 46, M. Bumrungron, K. Hirota, K. Takagi, K. Hanasaku, T. Hirai, I. Morioka, R. Yasufuku, M. Kitamura, and K. Hasezaki, Synthesis

resistivity and thermal conductivity. As a result, the obtained  $ZT$  of PbTe was found to be 0.8 at 300 K. The thermoelectric properties of Cu-doped p-type  $\text{Bi}_{0.5}\text{Sb}_{1.5}\text{Te}_3$  were investigated to determine the intrinsic excitation effect in BST material, resulting in the highest  $ZT$  of 1.0 at 450 K.<sup>156</sup> The layered compound  $\text{BiMnTe}_4$  was found to be a p-type semiconductor with a high Seebeck coefficient at 300 K (168  $\mu\text{V}/\text{K}$ ). Also, in nanostructured  $\text{Bi}_2\text{Te}_3/\text{MnTe}_2$ , the  $ZT$  was found to be 0.26 at 480 K.<sup>157</sup> The sintered bulk materials of p-type  $\text{Bi}_{0.52}\text{Sb}_{1.48}\text{Te}_3$  prepared using melt spinning and rapid sintering were found to depend on thermal conductivity of ambient gases with enhancement in  $ZT$  value of about 1.09 at 340 K.<sup>158</sup> To control the crystallographic preferred orientation, melt spinning method has been applied for  $\text{CHI}_3$ -doped  $\text{Bi}_2\text{Te}_{2.4}\text{Se}_{0.6}$  alloys with an optimized frequency of 300 rpm with  $ZT$  of 1.02 at 400 K.<sup>119</sup> The outstanding homogeneity and reproducibility by varying the stoichiometry have played a crucial role in the transport properties of p-type  $\text{Bi}_x\text{Sb}_{2-x}\text{Te}_3$  prepared by melt spinning.<sup>159</sup> The bulk materials of p-type  $\text{Bi}_{0.52}\text{Sb}_{1.48}\text{Te}_3$  were synthesized by Yun et al.,<sup>160</sup> and it was observed that an argon atmosphere could effectively inhibit heat loss

and thermoelectric properties of bismuth antimony telluride thermoelectric materials fabricated at various ball-milling speeds with yttria-stabilized zirconia ceramic vessel and balls, 13869. Copyright (2020), with permission from Elsevier.<sup>149</sup>

and suppress the sublimation of tellurium. Therefore, the  $\text{Bi}_{0.52}\text{Sb}_{1.48}\text{Te}_3$  sample showed the highest  $ZT$  of 1.09 at 340 K (Fig. 13a, b, c, and d). The secondary phase of  $\text{NiTe}_2$  and  $\text{NbTe}_2$  in a p-type  $\text{Bi}_{0.5}\text{Sb}_{1.5}\text{Te}_3$  thermoelectric was investigated by Kim et al.<sup>161</sup>  $\text{Bi}_{0.5}\text{Sb}_{1.5}\text{Te}_3(\text{NiTe}_2)_{0.01}$  and  $\text{Bi}_{0.5}\text{Sb}_{1.5}\text{Te}_2(\text{NbTe}_2)_{0.01}$  exhibited a  $ZT$  of 0.98 and 0.94 at 300 K, respectively (Fig. 14a, b, c, and d).

The SHS technique is a combustion method for synthesizing thermoelectric materials. It was systematically evaluated by varying the thermodynamic and kinetic parameters for n-type  $\text{Bi}_2\text{Se}_{2.4}\text{Te}_{0.6}$  with reduced cost. A  $ZT$  of 0.95 was observed at 424 K and was 25% greater than melt-grown samples.<sup>125</sup> Bulk samples of n-type  $\text{Bi}_2\text{Te}_3$  fabricated by stacking 75 layers on top of each other has shown an electrical conductivity of  $122 \text{ S cm}^{-1}$ , Seebeck coefficient of  $-105.7 \mu\text{V}/\text{K}$ , and a  $ZT$  of 0.3 at 450 K.<sup>113</sup> An investigation of the thermoelectric performance of  $\text{Bi}_2\text{Se}_{3-x}\text{Te}_x$  ( $x = 0, 0.3, 0.6, 0.9$  and  $1.5$ ) prepared by SHS reported a power factor of  $11 \mu\text{W}/\text{mK}$ . The thermoelectric figure of merit was found to be enhanced by the low lattice thermal conductivity and calculated to be 0.67 at 483 K for  $\text{Bi}_2\text{Se}_{1.5}\text{Te}_{1.5}$ .<sup>162</sup> Further, a self-propagating high-temperature technique was

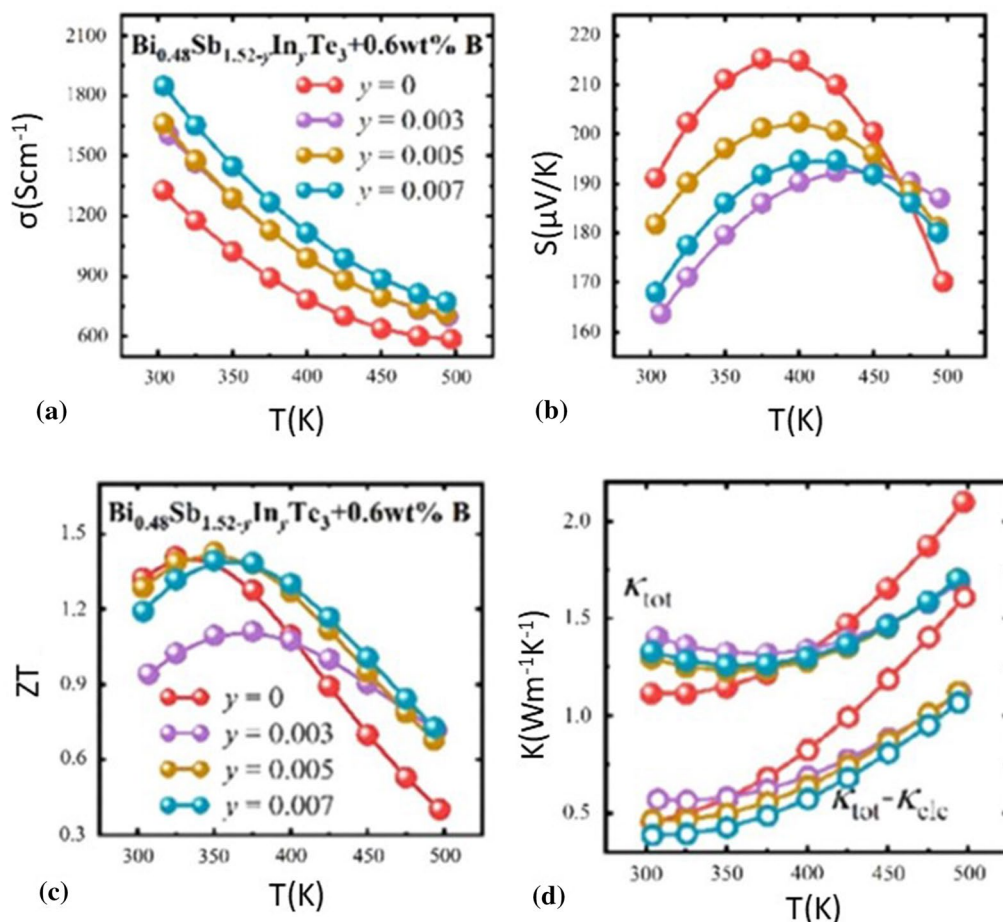


**Fig. 11** Temperature-dependent (a) electrical resistivity, (b) Seebeck coefficient, (c)  $ZT$  value, and (d) total thermal conductivity of  $\text{Bi}_{0.48}\text{Sb}_{1.515}\text{In}_{0.005}\text{Te}_3 + 0.6 \text{ wt}\%$  boron-doped samples. Reprinted from *Chemical Engineering Journal*, 429, H. Wang, G. Wu, Z. Yan,

X. Tan, J. Cai, H., Peng, S., Liu, G. Jiang, Synergistic Effects of B-In Codoping in Zone-Melted  $\text{Bi}_{0.48}\text{Sb}_{1.52}\text{Te}_3$ -Based Thermoelectric, 130381, Copyright (2021) with permission from Elsevier.<sup>153</sup>

used to prepare  $\text{Bi}_2\text{Se}_{3-x}\text{Te}_x$ , where Se vacancies and antisite defects resulted in a carrier concentration of  $2 \times 10^{19} \text{ cm}^{-3}$ . Hence, there is a suppression in lattice thermal conductivity from 1.07 W/mK to 0.61 W/mK at 300 K, and a  $ZT$  of 0.67 at 473 K has been achieved for  $\text{Bi}_{0.5}\text{Sb}_{1.5}\text{Te}_3$ .<sup>163</sup> Textured  $\text{BiSbTe}_{1.5}\text{Se}_{1.5}$  was prepared by Oleg et al.<sup>164</sup> They achieved a maximum  $ZT$  of 0.43 at 500 K using self-propagation high-temperature technique. The texturing resulted in anisotropy in the specific electrical conductivity and thermal conductivity, as represented in Fig. 15a, b, c, and d.

Single-phase nanopowders were synthesized using the hydrothermal method where  $\text{BiCl}_3$  and  $\text{SbCl}_3$ , and Te powders were used as precursors. The presence of a thermal difference probably enhanced the directional arrangement of nanosheets of  $\text{Bi}_{0.5}\text{Sb}_{1.5}\text{Te}_3$ , which is advantageous for improving the thermoelectric properties. The highest figure of merit was found to be 0.86 at 373 K.<sup>165</sup> The Seebeck coefficient of prepared polythiophene ( $P_{\text{Th}}$ )/ $\text{Bi}_2\text{Te}_3$  was determined to be negative over the whole temperature range, and

the highest value was found to be  $130 \mu\text{V/K}$ . The decrease in carrier concentration and electrical resistivity was due to the poor conductivity of the polymer, which resulted in a  $ZT$  of 0.17 at 473 K.<sup>166</sup> A widely used and facile hydrothermal approach was carried out for bismuth telluride nanorods with nanoplates stacks. Based on the titration, composition of the alloys was determined to be  $\text{Bi}_2\text{Te}_{2.4}$ . The two types of sintering technologies of high pressure/high-temperature (HPHT) and SPS were organized to prepare a  $\text{Bi}_2\text{Te}_3$  alloy, which shows  $ZT$  values of 0.47 and 0.42 for HPHT and SPS, respectively, at 430 K.<sup>167</sup> Besides, the thermoelectric properties of nanostructured La-doped  $\text{Bi}_2\text{Te}_3$  compound prepared by hydrothermal technique were investigated. The compound exhibited a flower-like structure due to the assembly of nanosheet crystals. The defects strongly affected the compound, and the highest  $ZT$  value of 0.4 at 550 K was shown by the pristine sample.<sup>168</sup> Bismuth telluride is assembled by nanosheets and synthesized by solvothermal route. The large compatible plane structure, reduction of nucleation, and

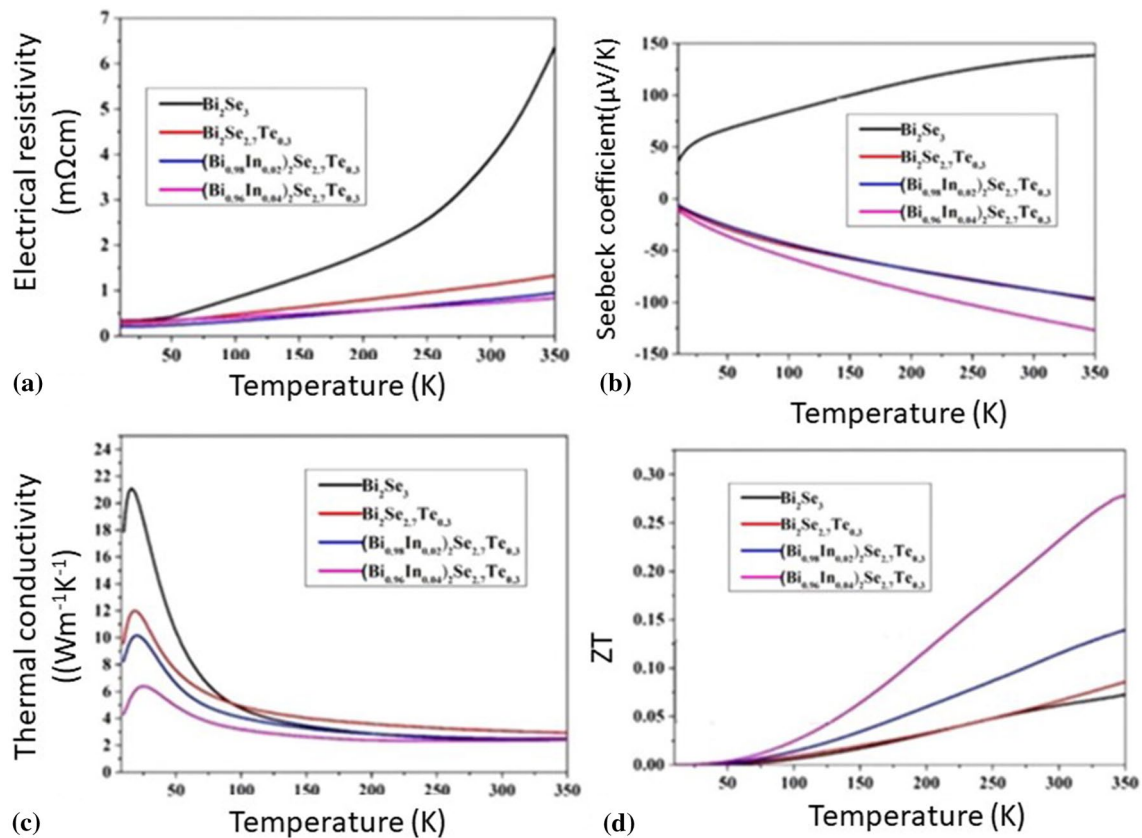


**Fig. 12** Temperature-dependent (a) electrical resistivity, (b) Seebeck coefficient, (c) total thermal conductivity, and (d)  $ZT$  value of single-crystal  $(\text{Bi}_{0.96}\text{In}_{0.04})_2\text{Se}_{2.7}\text{Te}_{0.3}$  samples. Reprinted from *Journal of Alloys and Compounds*, 866, G. S. Hegde, A. N. Prabhu, Y.

H. Gao, Y. K. Kuo, and V. R. Reddy, Potential thermoelectric materials of indium and tellurium co-doped bismuth selenide single crystals grown by melt growth technique, 158814, Copyright (2020) with permission from Elsevier. <sup>126</sup>

interfacial angle energies are responsible for the generation of defects. Hence, to assess the influence of the defects on their thermoelectric performance, bulk pellets were examined, and they showed a  $ZT$  value of 0.68.<sup>169</sup> Rini Singh et al. demonstrated an easy and economical wet chemical route for the preparation of bismuth telluride nanostructures. Bismuth telluride was studied with only preliminary investigations; the samples exhibited rhombohedral (R-3m) and hexagonal (P-3 m1) phases. All the XRD peaks could be indexed well with  $\text{Bi}_2\text{Te}_3$  and  $\text{BiTe}$  phases. Some of the peaks represent the formation of oxide. The nanocrystals of  $\text{Bi}_2\text{Te}_3$  were fabricated using a colloidal nanoplate technique. The crystals exhibited a highest power factor of  $0.35 \text{ m Wm}^{-1} \text{ K}^{-2}$  at 433 K, which is among the highest reported values for flexible thermoelectric films.<sup>170</sup> High-purity bismuth telluride ( $\text{Bi}_2\text{Te}_3$ ) nanostructures have been synthesized using coprecipitation and annealing process. The study of thermoelectric properties of  $\text{Bi}_2\text{Te}_3$  nanostructure in synthesis ( $\text{HNO}_3\text{-Bi\&Te}$ ) showed a maximum value of thermoelectric voltage of 21 mV at a temperature difference of 90 K. The amount of  $ZT$  obtained in the co-precipitated bismuth

telluride was found to be enhanced by 6.5 times compared to the annealing method.<sup>171</sup>

$\text{Bi}_2\text{Te}_3$  nanoparticles were fabricated by a microwave-assisted chemical synthetic route with tartrate complexes  $\text{Bi}^{3+}$  and  $\text{Te}^{4+}$ . The nanoparticles exhibited a higher Seebeck coefficient ( $-135 \mu\text{V}\text{K}^{-1}$ ), lower thermal conductivity ( $0.957 \text{ W/mK}$ ), and a dimensionless figure of merit of 1.0 at 300 K.<sup>172</sup> The effect of microwave processing was examined to determine the optimal thermoelectric performance of  $(\text{Bi}_x\text{Sb}_{1-x})_2\text{Te}_3$ /ethylene glycol 2964 (EG) alloy at room temperature. EG insertion enhanced the Seebeck coefficient, and a  $ZT$  of 1.2 was obtained at 300 K.<sup>173</sup> This technique was utilized in a comparative study of  $\text{Bi}_{2-x}\text{Sb}_x\text{Te}_3$  prepared by mechanochemical alloying and microwave (MW) synthesis routes, where a hexagonal platelet morphology was observed. Microwave-synthesized samples showed thermal conductivity less than that obtained by the alloying method, with  $ZT$  values of 1.0 and 0.6 obtained at 440 K for the microwave route and mechanochemical alloying, respectively.<sup>174</sup> The microwave technique was also adopted to synthesize thermoelectric

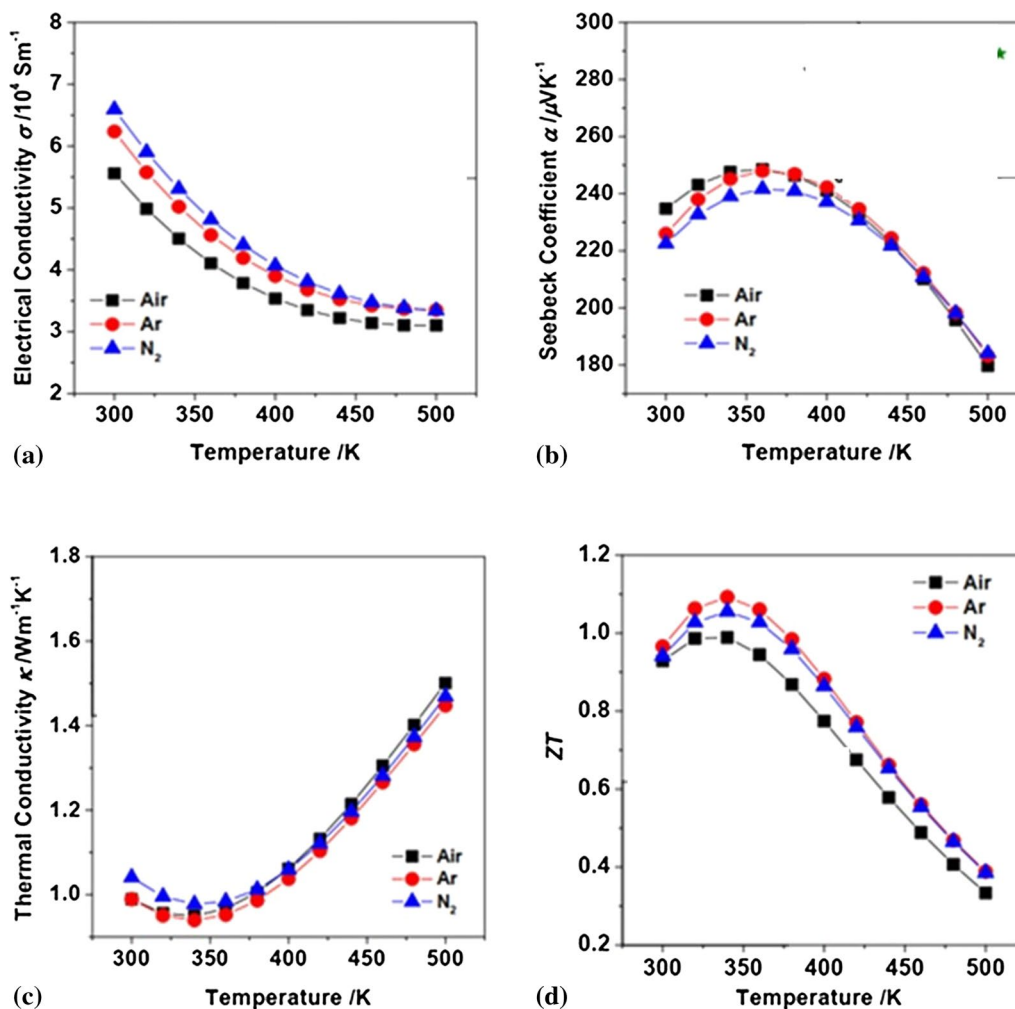


**Fig. 13** Temperature-dependent (a) electrical resistivity, (b) Seebeck coefficient, (c) total thermal conductivity, and (d)  $ZT$  value of single-crystal  $\text{Bi}_{0.52}\text{Sb}_{1.48}\text{Te}_3$  samples. Adapted from *ACS Applied Materials & Interfaces*, 12, Y. Zheng, H. Xie, Q. Zhang, A. Suwardi, X. Cheng, Y. Zhang, W. Shu, X. Wan, Z. Yang, Z. Liu, and X. Tang, Unravel-

ling the critical role of melt-spinning atmosphere in enhancing the thermoelectric performance of p-type  $\text{Bi}_{0.52}\text{Sb}_{1.48}\text{Te}_3$  alloys, 36186. Copyright (2020) with permission from the American Chemical Society.<sup>158</sup>

nanopowders of a  $\text{Bi}_{2-x}\text{Sb}_x\text{Te}_3$  system. A unique transition was observed from p- to n-type semiconducting with  $ZT$  values of 1.04 and 0.4, respectively, for the n and p types at 448 K.<sup>175</sup>

Ahmed et al.<sup>176</sup> used spark plasma sintering for the preparation of n-type  $(\text{Bi}_{0.95}\text{Sb}_{0.05})_2(\text{Se}_{0.05}\text{Te}_{0.95})$ . The Seebeck coefficient was found to increase by 12% relative to the sample prepared by dry conditioning. The simultaneous reduction in electrical resistivity and thermal conductivity observed in the sample prepared by SPS led to an enhanced  $ZT$  value (0.63 at 420 K) by 21% as compared to that of the dried mixture (Fig. 16a, b, c, and d). The spark plasma sintered thermoelectric compound  $\text{Bi}_{0.5}\text{Sb}_{1.5}\text{Te}_3$  showed the lowest thermal conductivity of 0.85 W/mK, electrical conductivity of 4.48 S/cm, and the highest  $ZT$  of 1.03 at 300 K.<sup>177</sup>

Nanopowders of selenium and lutetium co-doped  $\text{Bi}_2\text{Te}_3$  are synthesized by hydrothermal method and are sintered using spark plasma sintering technique. By doping of Se into Lu-doped  $\text{Bi}_2\text{Te}_3$ , the electrical conductivity of  $\text{Lu}_{0.1}\text{Bi}_{1.9}\text{Te}_{3-x}\text{Se}_x$  material is found to decrease with the increase in Se content due to the reduced carrier concentration, while the Seebeck coefficient values are observed to be enhanced. The huge reduction in the lattice thermal conductivity of  $\text{Lu}_{0.1}\text{Bi}_{1.9}\text{Te}_{3-x}\text{Se}_x$ , ascribed to point defects and fluctuation of atomic mass, results in a maximum  $ZT$  value of 0.85 at 420 K. Powders of high entropy and single-phase nanosized  $(\text{BiSbSe}_{1.5}\text{Te}_{1.5})_{1-x}\text{Cu}_x$  compound with concentration  $x = 0, 0.3, 0.6$  were prepared by soft chemical reaction, due to its low thermal conductivity, and the compound was found to be favorable for thermoelectric applications.<sup>178</sup> Hamawandi et al.<sup>179</sup> reported

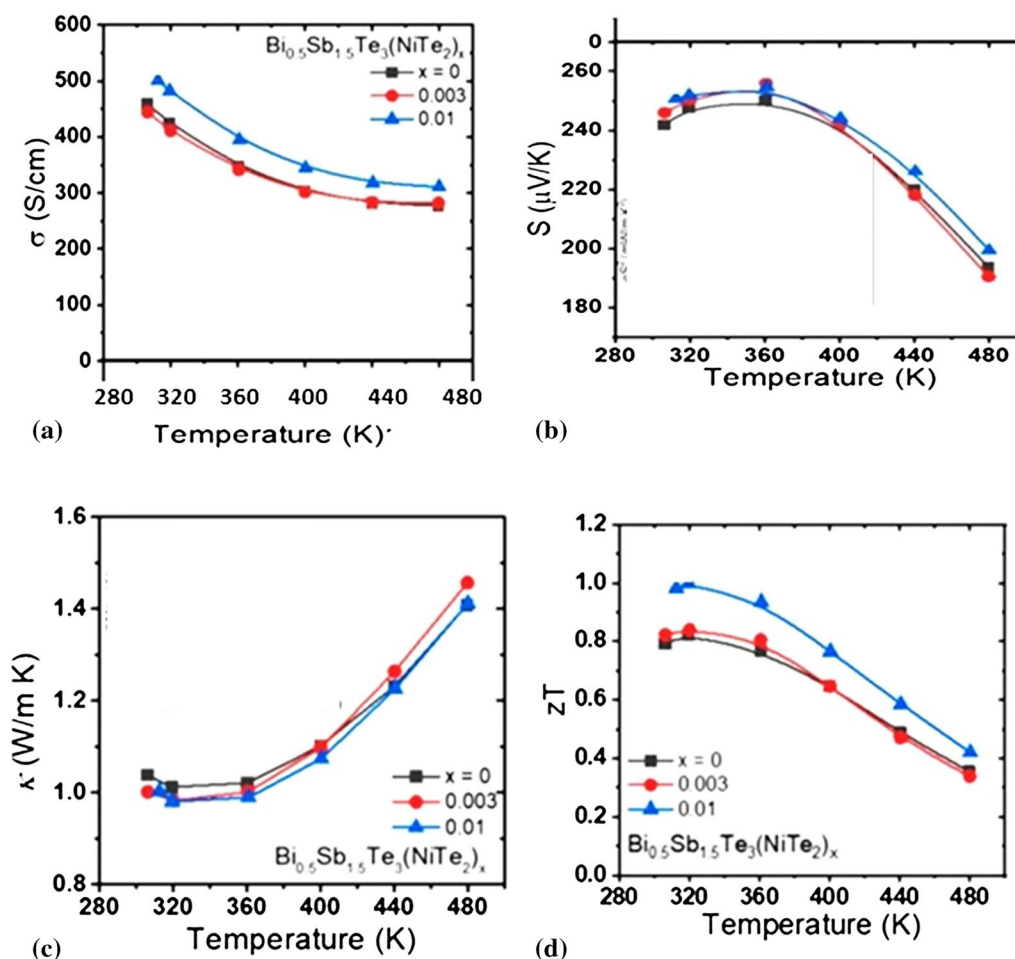


**Fig. 14** Temperature-dependent (a) electrical resistivity, (b) Seebeck coefficient, (c) total thermal conductivity, and (d)  $ZT$  value of  $\text{Bi}_{0.5}\text{Sb}_{1.5}\text{Te}_3(\text{NiTe}_2)_{0.01}$ . Adapted from *Applied Science*, 11, H.-S. Kim, T. Kim, J. An, D. Kim, J. H. Jeon, and S. Kim, Segregation of

$\text{NiTe}_2$  and  $\text{NbTe}_2$  in p-Type Thermoelectric  $\text{Bi}_{0.5}\text{Sb}_{1.5}\text{Te}_3$  Alloys for Carrier, Energy Filtering Effect by Melt Spinning, 910. Copyright (2021) with permission from MDPI under CC by license.<sup>161</sup>

two forms of bismuth telluride synthesized by a hydro and polyol method, where the final forms of samples prepared by both methods were subjected to spark plasma sintering. Using the hydro method, the electrical conductivity values, Seebeck coefficient, thermal conductivity, and  $ZT$  were found to be  $9.6 \times 10^5$  S/m,  $-149$   $\mu\text{V/K}$ ,  $0.9$  W/mK, and  $0.88$ , respectively, at  $373$  K, whereas they were  $9.2 \times 10^5$  S/m,  $-148$   $\mu\text{V/K}$ ,  $0.86$  W/mK, and  $0.86$ , respectively, at  $373$  K using the polyol method (Fig. 17a, b, c, and d). Hong et al. synthesized the  $\text{SbI}_3$ -doped  $95\%$   $\text{Bi}_2\text{Te}_3$  and  $5\%$   $\text{Bi}_2\text{Se}_3$  compounds using quick solidification and extrusion between  $420^\circ\text{C}$  and  $480^\circ\text{C}$ . The hot-extruded compounds exhibited Seebeck coefficient values of  $160.8$ ,  $170.2$ , and  $165.7$   $\text{mV/K}$  at  $420$ ,  $450$ , and  $480^\circ\text{C}$  respectively. The electrical resistivity for the compounds at  $420$ ,  $450$ , and  $480^\circ\text{C}$  was found to be  $0.49$ ,  $0.57$ , and  $0.51$   $\Omega\text{m}$ , respectively. The maximum power factor value of the compound at  $480^\circ\text{C}$  was  $53.8 \times 10^6$   $\text{mW cm}^{-2} \text{K}^{-2}$ .<sup>130</sup> Soon

lim et al. proposed the hot extrusion technique for ZnO-encapsulated  $\text{Bi}_2\text{Te}_{2.7}\text{Se}_{0.3}$  alloys to determine the thermoelectric properties. The electrical resistivity, Seebeck coefficient, and  $ZT$  values were found to be  $2 \times 10^5$  S/m,  $-150$   $\mu\text{V/K}$ , and  $0.7$ , respectively.<sup>131</sup> Jung et al. introduced the hot extrusion method to fabricate high-performance n-type thermoelectric bismuth tellurium selenides. It was observed that electrical conductivity of  $33,333$  S/m was obtained for a sample prepared at  $2.40$  Mpa and  $480$  K, whereas the highest  $ZT$  value and Seebeck coefficient of  $0.8$  and  $200$   $\mu\text{V/K}$ , respectively, were found at  $480$  K.<sup>132</sup> N-type  $(1-x)\text{Bi}_2\text{Te}_{3-x}\text{Bi}_2\text{Se}_3$  alloys with various composition and electron density were investigated by Jung et al. using the hot extrusion method. The donor dopant used was  $\text{SbI}_3$  to control the electron density of the samples in  $10^{19} \text{cm}^{-3}$  range.  $0.85\text{Bi}_2\text{Te}_3-0.15\text{Bi}_2\text{Se}_3$  shows electrical resistivity, Seebeck coefficient, and power factor values



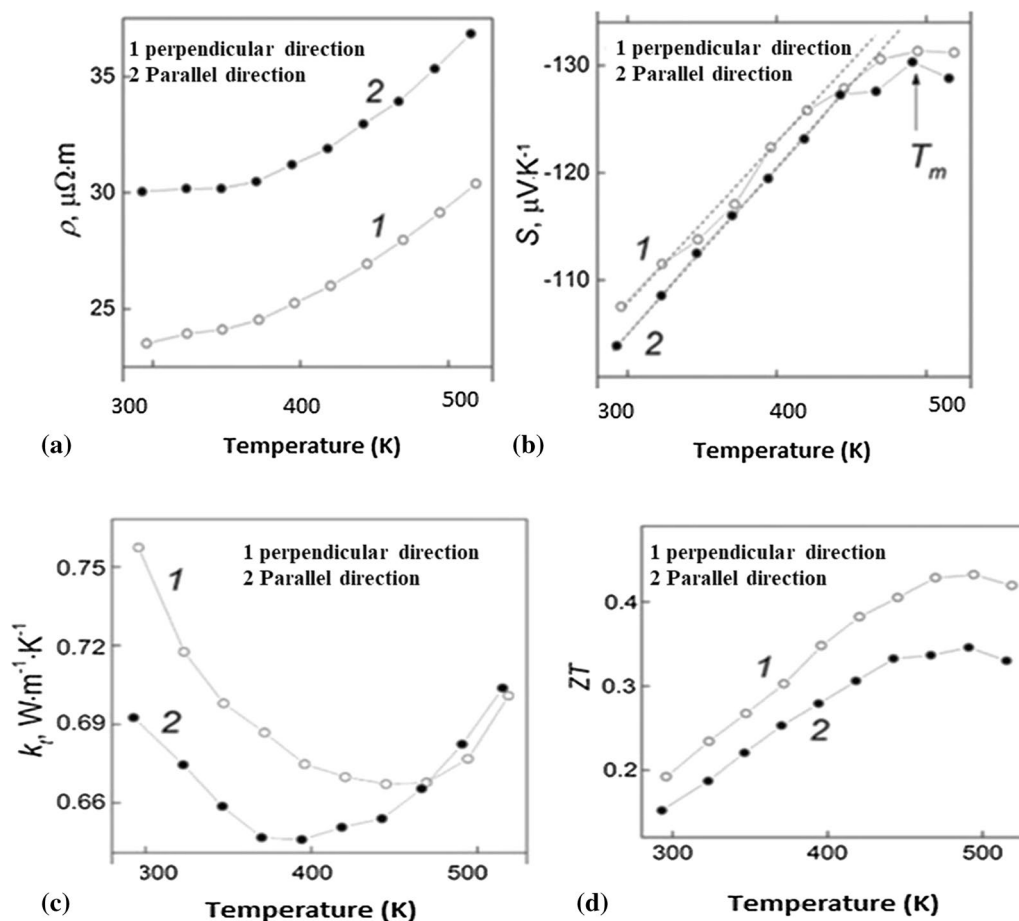


**Fig. 15** Temperature-dependent (a) electrical resistivity, (b) Seebeck coefficient, (c) total thermal conductivity, and (d) ZT value of BiSbTe<sub>1.5</sub>Se<sub>1.5</sub>. Reprinted from *Journal of Alloys and Compounds*, 872, O. Ivanov, M. Yaprntsev, A. Vasilev, E. Yaprntseva, Micro-

structure and thermoelectric properties of the medium-entropy block-textured BiSbTe<sub>1.5</sub>Se<sub>1.5</sub> alloy, 159743. Copyright (2021) with permission from Elsevier.<sup>164</sup>

of 300,000 S/m,  $-300 \mu\text{V}/\text{K}$ , and  $3.5 \times 10^{-3} \text{ W}/\text{mK}^2$ , respectively.<sup>180</sup>

### Effect of Point Defect and Effective Mass ( $m^*$ ) on Carrier Transport Phenomenon and Density of States (DOS)

Bismuth chalcogenide compounds have two primary defects, lines and points in the lattice, as an effect of quenching. The line defect is considered to be dislocation, which decreases the mobility of the charge carriers. Further, single crystals are tilted strongly through the parallel axis to the basal plane. The point defect generated at high temperature during sintering or growth can be quenched in the sample at a lower temperature. The point defects in chalcogenide compounds are mainly of three types: (a) Frankel defect (b) Schottky–Wagner defect, and (c) antistructure defect. These defects can act as an acceptor/donor with regard to the levels of energy

associated with the Fermi level. In bismuth chalcogenides, the acceptor levels lie in the valence band, and donor levels lie in the conduction band. As a result, the defects are subjected to ionization throughout the temperature range. The impact of vacancies formed through plastic deformation in n-type Bi<sub>2</sub>Te<sub>3</sub> and Bi<sub>2</sub>Se<sub>3</sub> decreases the mobility of carriers while leaving the charge carriers unaffected due to ionized vacancy scattering. Ionization is established by the bond rearrangement of electrons rather than the trapping of conduction holes and electrons.<sup>181</sup> Point defect engineering is an effective tool for enhancing thermoelectric bismuth chalcogenide-based alloys by regulating the content of dopants like Sb, In, and Sn in Bi<sub>2</sub>Te<sub>3</sub> and Bi<sub>2</sub>Se<sub>3</sub> based on minor differences in electronegativity.<sup>70</sup>

In some cases, the effective mass of a material results in higher valley degeneracy at a low- to near-room-temperature range. The significant contribution to carrier transport comes from the position of the Fermi level ( $E_F$ ) from the conduction energy band ( $E_C$ ) in an n-type semiconductor and the

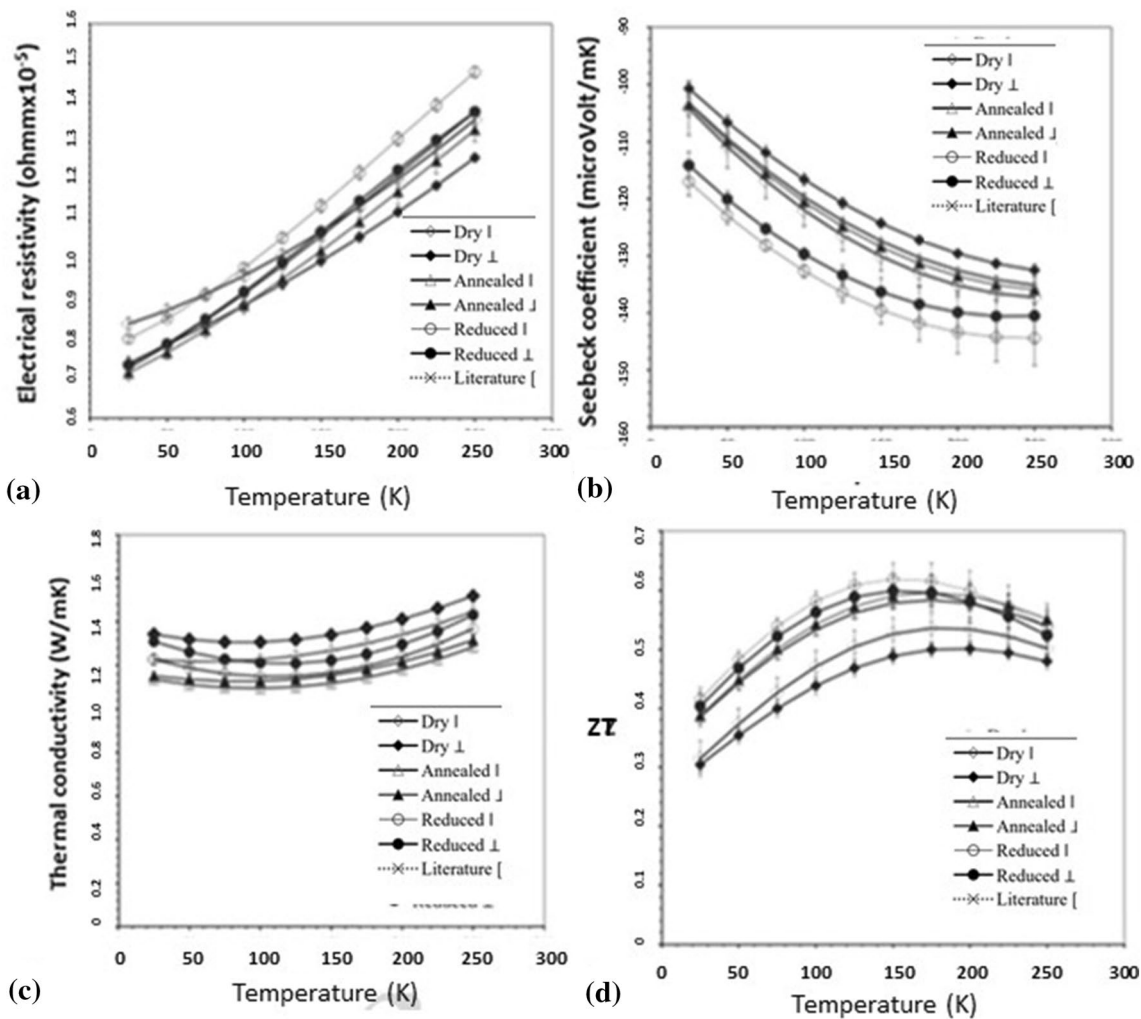


**Fig. 16** Temperature-dependent (a) electrical resistivity, (b) Seebeck coefficient, (c) total thermal conductivity, and (d)  $ZT$  value of  $(\text{Bi}_{0.95}\text{Sb}_{0.05})_2(\text{Se}_{0.05}\text{Te}_{0.95})$ . Reprinted from *Journal of Alloys and Compounds* 874, A. A. Abdelnabi, V. Lakhian, J. R. McDermid, The

effect of powder pre-treatment on the mechanical and thermoelectric properties of spark plasma sintered N-type bismuth telluride, 159782. Copyright (2021) with permission from Elsevier.<sup>176</sup>

valence energy band ( $E_v$ ) in the case of a p-type semiconductor. Thermoelectric power increases with an increase in  $E_C - E_F$ , which helps increase weighted mobility and thermopower. The substitutional alloys display a larger energy gap than binary compounds by suppressing minority charge conduction at high temperatures. The high weighted mobility in bismuth chalcogenides is mainly due to its complex Fermi surface, which generates six valley conducting bands.<sup>182</sup>

Burai Quantum ESPRESSO software is used to determine the density of states (DOS) and Fermi energy of  $\text{Bi}_2\text{Te}_3$ ,  $\text{Bi}_2\text{Se}_3$ , and In/Sb/Sn-doped  $\text{Bi}_2\text{Te}_{2.7}\text{Se}_{0.3}/\text{Bi}_2\text{Se}_{2.7}\text{Se}_{0.3}$ . The simulated DOS of  $\text{Bi}_2\text{Te}_3$  and  $\text{Bi}_2\text{Se}_3$  are shown in Fig. 18a and b, which shows the electronic contribution from several atoms. The valence band is basically controlled by the 5p state of the tellurium atom. The conduction band comprises both 6p Bi and 5p Te states with short tight bonds. First,

the second and fourth atomic layers have zero density of state and have a gap in the Fermi level.<sup>183</sup> Each atom of  $\text{Bi}_2\text{Te}_3$  and  $\text{Bi}_2\text{Se}_3$  participates in the formation of a Dirac cone.  $P_z$  states of bismuth atoms have the greatest influence on the formation of the surface state with linear dispersion, whereas a minor contribution is observed from selenium and tellurium atoms in  $p_x$  and  $p_y$  orbitals. The density of states provides evidence regarding the derivation of bands in the instance of  $\text{Bi}_2\text{Te}_3$ . The s orbital of Bi, and Te-1 and Te-2 atoms contribute the most states to core bands, while p orbitals of Te/Se-1 and Te/Se-2 contribute the most states to the valence bands. From p orbitals, the calculations of band structures and the total density of states, we obtain an energy gap value of around 6.79 eV for  $\text{Bi}_2\text{Se}_3$ ; conversely, for  $\text{Bi}_2\text{Te}_3$ , the band gap is calculated as 7.0 eV (Table II). The dopant elements indium, tin, antimony (cations), and

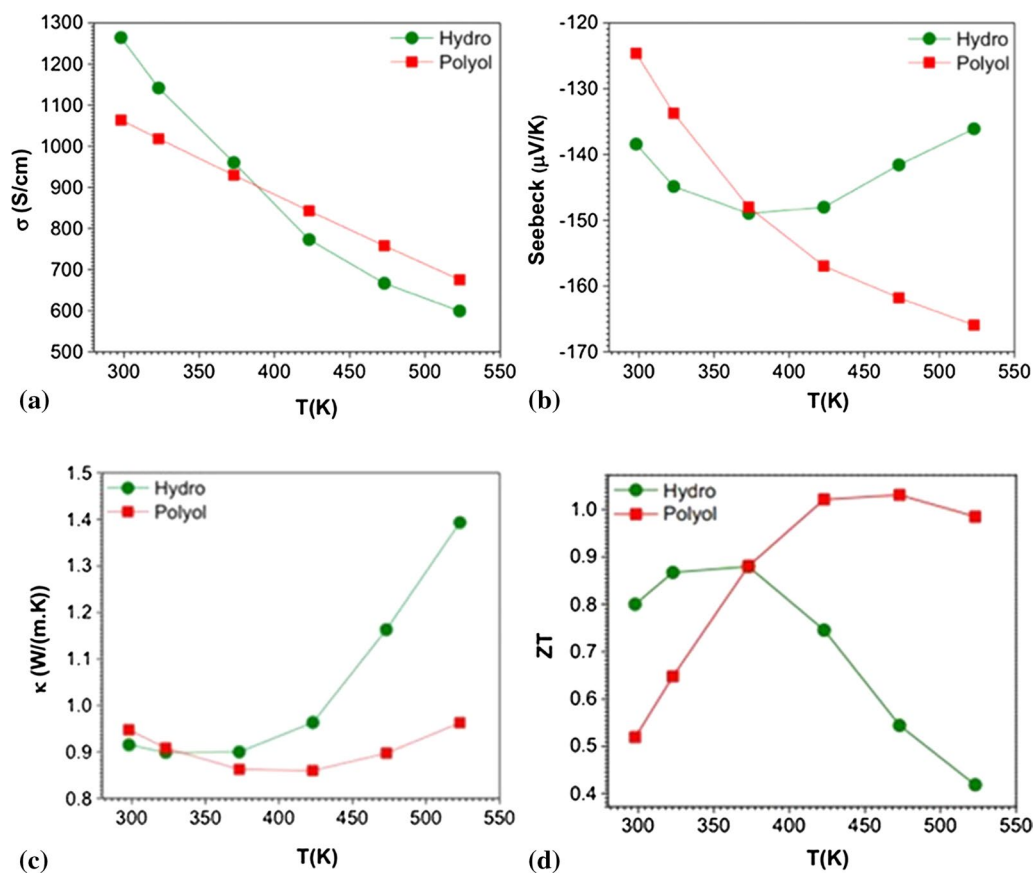


**Fig. 17** Temperature-dependent (a) electrical resistivity, (b) Seebeck coefficient, (c) total thermal conductivity, and (d)  $ZT$  value of polyol and hydro bismuth telluride. Reprinted from *Nanomaterials*, 4, Hamawandi B, Batili H, Paul M, Ballikaya S, Kilic NI, Szukiewicz

R, Kuchowicz M, Johnsson M, Toprak MS, Minute-Made, High-Efficiency Nanostructured  $\text{Bi}_2\text{Te}_3$  via High-Throughput Green Solution Chemical Synthesis, 2053. Copyright (2021), with permission from MDPI under CC by license.<sup>179</sup>

selenium and tellurium (anions) were selected based on their ionic radius and the similar properties of their outer shells. Sn, In, and Sb are known to be unique cases of resonant impurities in  $\text{Bi}_2\text{Te}_3$  and  $\text{Bi}_2\text{Se}_3$  semiconductors.<sup>184</sup> The doping of different elements causes a rigid shift of the Fermi level. The resonance level (RL) has different effects on the electronic and transport performance of a base compound, depending on its position and band edges, and it acts as a charge trap when it is in the strong resonant scattering center. These alloys form defect states pin the Fermi level and promote the partial charge localization. By considering the perspective of semiconductors based on thermoelectric materials, the RL is close to the band edge and hybridizes with the host electronic states around a valence band. Therefore, this condition could increase the Seebeck coefficient and  $ZT$  value of the materials. It is noted that high defect states are the cause for the acceptor-like behavior of dopants In, Sn, and Sb in bismuth.<sup>185</sup>

From Fig. 18c and d, it is realized that the energy peak at  $-0.96$  eV is primarily created by indium  $5s$  and  $6p$  states of bismuth. The  $s$ -state of Bi receives few electrons from

indium in the DOS region of 1.5 eV. At the resonance level, the impurity state coincides with the band energy of the host atoms, unlike the normal dopant state, where the impurity energy falls within that resonant peak in the valence band. This can be attributed to the  $s$  orbital of the dopant. The density of states of Sb-doped  $\text{Bi}_2\text{Te}_{2.7}\text{Se}_{0.3}$  and  $\text{Bi}_2\text{Se}_{2.7}\text{Te}_{0.3}$  has been shown in Fig. 18e and f. In order to fill  $sp^3d^2$  hybrid, an electron from the  $p$  orbital of Te<sup>(1)</sup> and Se<sup>(1)</sup> shifts to the Bi metal atom. The sharp resonant peak is observed at 0.95 eV of the DOS near the edge of the valence band in Sn-doped  $\text{Bi}_2\text{Te}_{2.7}\text{Se}_{0.3}$ , whereas,  $s$ -like behavior is observed in the orbital moment of the DOS peak. The resonant level is formed in the  $5s$  orbital of Sn, as shown in Fig. 18g and h.<sup>186</sup> With progression of the DOS and Fermi level with insertion of Sn concentration and Se/Te,  $n$ - $p$  crossover takes place. Therefore, Sn compensates the donor vacancy effect. Hence, by observing these phenomena, it seems that the effective way of controlling the Fermi level is co-doping. The theoretically simulated Fermi energy has been calculated and given in Table II.

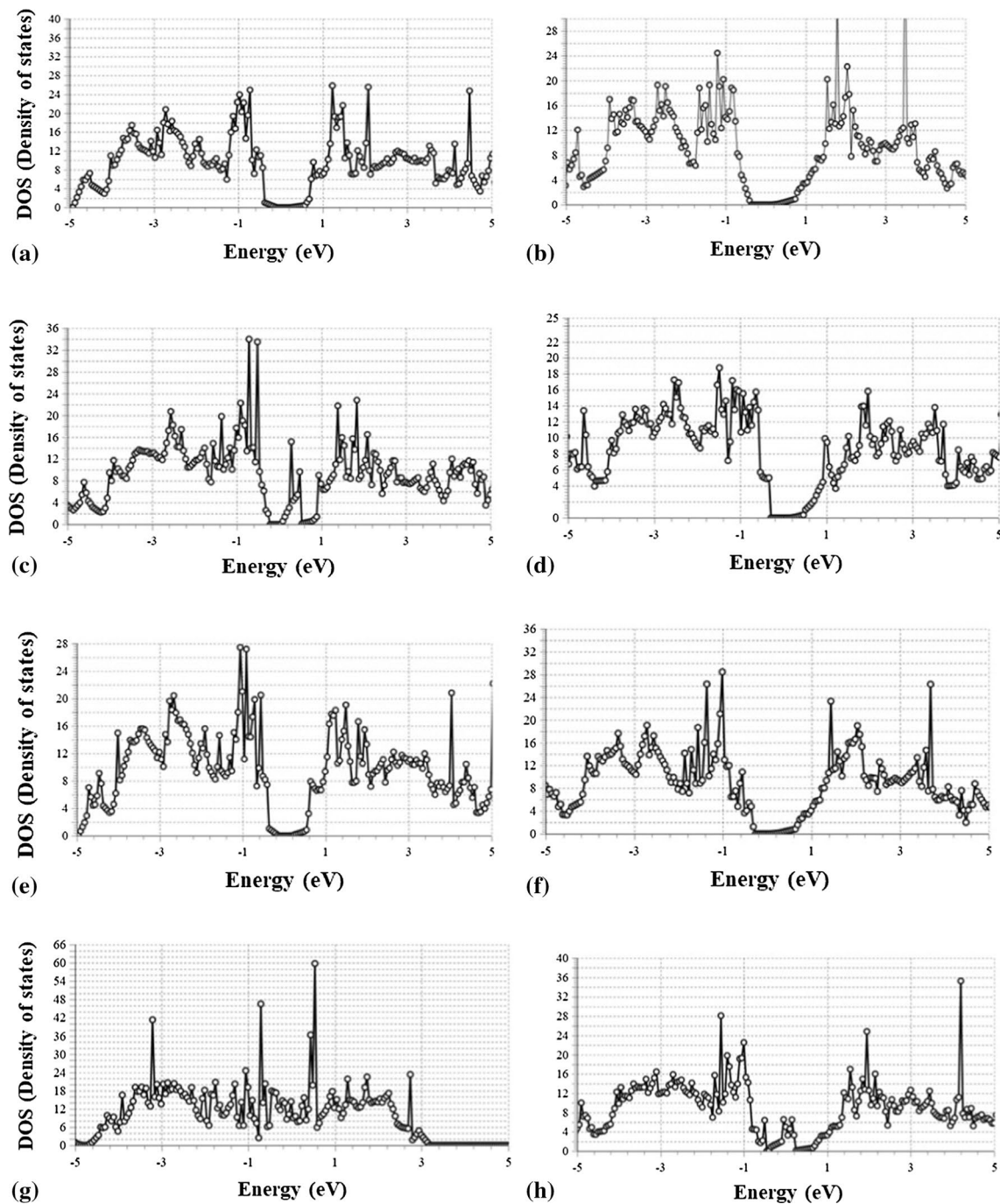


**Fig. 18** Simulated density of states of (a)  $\text{Bi}_2\text{Te}_3$ , (b)  $\text{Bi}_2\text{Se}_3$ , (c)  $(\text{Bi}_{1-x}\text{In}_x)_2\text{Te}_{2.7}\text{Se}_{0.3}$ , (d)  $(\text{Bi}_{1-x}\text{In}_x)_2\text{Se}_{2.7}\text{Te}_{0.3}$ , (e)  $(\text{Bi}_{1-x}\text{Sb}_x)_2\text{Te}_{2.7}\text{Se}_{0.3}$ , (f)  $(\text{Bi}_{1-x}\text{Sb}_x)_2\text{Se}_{2.7}\text{Te}_{0.3}$ , (g)  $(\text{Bi}_{1-x}\text{Sn}_x)_2\text{Te}_{2.7}\text{Se}_{0.3}$ , and (h)  $(\text{Bi}_{1-x}\text{Sn}_x)_2\text{Se}_{2.7}\text{Te}_{0.3}$ .

### Use of $\text{Bi}_2\text{Te}_3$ and $\text{Bi}_2\text{Se}_3$ Material as a Device

The thermoelectric properties of bismuth chalcogenides were verified by Thomas Seebeck in 1822–1823 with the common Palestine minerals  $\text{Bi}_4\text{Te}_3$  and  $\text{Bi}_2\text{Se}_3$ . The Bi–Te binary system was found to possess a large Seebeck coefficient. The Bi–Te/Se binary is classified into p and n types

based on whether it is prepared using Bi-rich or Te composition.<sup>187</sup> When there was an availability of both n-type and p-type  $\text{Bi}_2\text{Te}_3$ , greater cooling of  $40^\circ\text{C}$  was attained in 1955<sup>188</sup> and was again increased to  $65^\circ\text{C}$  by Sheard et al.<sup>189</sup> The optimization of thermoelectric properties of bismuth chalcogenides was carried out by Loffe et al.<sup>190</sup> Optimized alloys  $\text{Bi}_2\text{Te}_3$ – $\text{Bi}_2\text{Se}_3$  and  $\text{Bi}_2\text{Te}_3$ – $\text{Sb}_2\text{Te}_3$  having

very low thermal conductivity were prepared for device fabrication.<sup>40,191,192</sup> The most suitable single-stage Peltier cooler based on the compound  $\text{Bi}_2\text{Te}_3/\text{Se}_3$  shows the generation of maximum potential differences at temperatures of 75 K and 300 K for the cold and hot sides, respectively.<sup>193</sup> In contrast, multistage coolers have observed higher differences by evading compatibility factors.<sup>194</sup> By regulating the carrier concentration, the temperature difference can be increased by 9%.<sup>195</sup> The Carnot efficiency of commercially available power modules is about 13%.<sup>196</sup> As the power generator operates at elevated temperatures, there is a suppression of the bipolar effect. Hence, doping, alloying, and material processing are vital in improving the device quality of bismuth chalcogenides at a desired temperature.<sup>197</sup>

**Table II** Fermi energies of pristine and In/Sb/Sn-doped  $\text{Bi}_2\text{Te}_3$  and  $\text{Bi}_2\text{Se}_3$  compounds

S. no.	Compound	Fermi energy (eV)
1	$\text{Bi}_2\text{Te}_3$	7.0726
2	$\text{Bi}_2\text{Se}_3$	6.7959
3	$(\text{Bi}_{1-x}\text{In}_x)_2\text{Te}_{2.7}\text{Se}_{0.3}$	6.5452
4	$(\text{Bi}_{1-x}\text{In}_x)_2\text{Se}_{2.7}\text{Te}_{0.3}$	6.7269
5	$(\text{Bi}_{1-x}\text{Sb}_x)_2\text{Te}_{2.7}\text{Se}_{0.3}$	6.5807
6	$(\text{Bi}_{1-x}\text{Sb}_x)_2\text{Se}_{2.7}\text{Te}_{0.3}$	6.7011
7	$(\text{Bi}_{1-x}\text{Sn}_x)_2\text{Te}_{2.7}\text{Se}_{0.3}$	6.4802
8	$(\text{Bi}_{1-x}\text{Sn}_x)_2\text{Se}_{2.7}\text{Te}_{0.3}$	6.3002

## Thermoelectric Wearable Devices

Metabolic heat dissipation such as that occurring during running or walking is a valuable source of thermoelectric energy production. Harvesting of the energy is accomplished by transducers to generate electric power for domestic devices. For the comfort, robustness, and inter-device communication of all users, the design, fabrication, and evaluation of self-powered monitoring in enhanced wearable instruments have been sponsored by the National Science Foundation (NSF) since 2012.<sup>198</sup> In 1998, the first commercial thermoelectric wristwatch was developed with 300 mV of open-circuit voltage, 0.1% efficiency conversion, and 25  $\mu\text{W}$  output power over a temperature difference of 1.5°C.<sup>199</sup> Though wearable thermoelectric generators cannot offer sufficient power for more sophisticated power electronics, they can power lower-energy wearables. Using the heat from a more significant part of the body, the power can be enhanced. The significant advances in thermoelectric wristwatches were related to the TEGs, power organization, and heat transfer design.

To increase the power output of TEG instruments, attentive inspection is supposed to be given for the design of TEG instruments.<sup>200,201</sup> The factors consist of load-matching heat spreaders, filler material, and interconnection of metals and substrates.<sup>202–205</sup> The lateral heat lost through fillers reduces the temperature gradient and degrades the output power of the TEG.<sup>206</sup> For an instrument with a 10% fill factor of 0.3 W/mK thermal conductivity and 0.03 W/mK filler conductivity, there is equilibrium between the total thermal conductivity of the thermoelectric material and the filler. Thus,

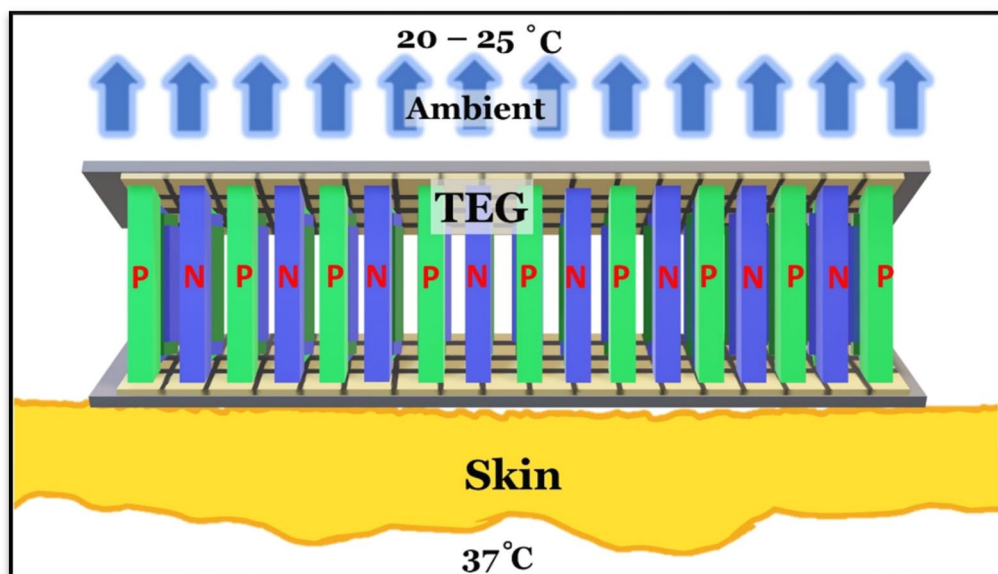


**Fig. 19** Schematic view of a TEG for body heat harvesting.

half of the heat is drained by the conduction in decreasing the output power.

Generally, a metal electrical interconnection is mounted on an insulating ceramic substrate (Fig. 19). These metal interconnections possess high electrical conductivity and corresponding thermal expansion, where they are made of gold-coated copper of thickness 20  $\mu\text{m}$ .<sup>207</sup> If TEG leg resistance is comparable to the contact of resistance, the interfacial resistance between the TEG legs and interconnections can bound the instrument performance. This phenomenon is possible only when contact resistance surpasses 10% of  $\frac{\rho L}{2}$  where  $\rho$  is electrical resistivity and  $L$  is the length of the TEG. The  $\rho$  of  $10^{-3}$   $\Omega$  cm and contact resistance of  $10^{-3}$   $\Omega$  cm<sup>2</sup>, and a leg length of more than 0.2 mm are the ideal factors for the TEG.<sup>208</sup> The interconnects in unbending TEGs are characteristically attached to a highly thermally conductive substrate of alumina ceramics.<sup>209</sup> The parasitic series thermal resistance is less than the resistance detected from the TEG. The resistance of the TEG can be increased by reducing the fill factor, which can be accomplished by decreasing the number of n- and p-type legs, increasing the aspect ratio of the legs, or decreasing the thermal conductivity of the legs.

TEG performance is limited by the skin–TEG interface and TEG–ambient interface. Human skin is called a thermal insulator, which creates the resistance between the core of a TEG and the body. The surface roughness of the skin is the reason for the contact resistance between the interface of the skin and TEG. The air–TEG interface resistance is frequently used if no heat sink is utilized on the upper part of the TEG. The contact pressure and the characteristics of the skin influentially modify this thermal resistance.<sup>183,210</sup> When the TEG is situated on body skin, the maximum power generated from a TEG decreases by 30%.<sup>211,212</sup>

Heat spreaders improve wearable TEG performance. The light weight and the flexibility are advantages of a heat spreader over a fin heat sink required for wearable applications. To improve the output power of the TEG hot and cold sides, heat spreaders are placed on either side of the TEG. To maximize the power generation, copper and carbon foils need to have 1000 W/mK and 400 W/mK of thermal conductivity and 100  $\mu\text{m}$  and 250  $\mu\text{m}$  of thickness, respectively.<sup>213</sup> Broadening the surface area of a spreader increases the power output up to a strong point, and the lateral thermal resistance is initiated to control the spreader role, which becomes less significant. The output power was amplified by 100% using a spreader of 16 mm<sup>2</sup>, which is very high compared to a TEG without a heat spreader. The temperature gradient and thermal resistance are found to reduce by increasing the number of TEG legs. For a human body TEG, the maximum temperature gradient is found to be less than 2°C with a fill factor of 10%.<sup>214</sup> The output power increases by increasing the aspect ratio, modifying the leg shape, and

lowering the fill factor across the module.<sup>210,211</sup> If a module has a fill factor in the range of 0.3% to 3%, it generates more power per unit area compared to instruments with a fill factor of more than 25%, whereas a module having a fill factor of less than 20% could compromise the integrity of mechanics.<sup>215–217</sup> The challenging process is TEG instrument fabrication and optimization of instrument parameters to boost converter output. Energy generation in a TEG is directly dependent on lowering the contact resistance of the module legs and maximization of the module steadiness in different environments.

## Future Challenges

By the end of 2022, the worldwide market for wearable technologies is predicted to exceed \$78 billion. The effectual body energy harvester unlocks the possibility of battery-less electronics of wearables to care for human health and ecological conditions. The wellness of health and user comfort will be monitored through thermoelectric watches, headbands, cuffs, innovative jewelry, and textiles. This digital and mobile health promises a reformed arrangement and distribution of medical care to authorize health teams to support patient monitoring and repossession. However, the output power levels are still low for practical applications, regardless of the effort to incorporate TEGs in textiles. Current TEGs have not been developed as thermoelectric instruments in materials science with the unparalleled efficiency of thermoelectricity.

## Conclusion

The review and summary of different processing aspects and their impact on thermoelectric properties of doped/composite bismuth chalcogenide materials have been discussed in this article. It is recognized that an appropriately doped and composite structure generally leads to enhanced thermoelectric performance. Mechanical alloying and high-energy ball milling are appropriate methods utilized in research laboratories and are easily scaled up in industries. In some cases, the development of compositional homogeneity can be obtained by melting/pulverizing processes carried out using ball milling for the resultant extracts. The soft chemical reaction method is employed to synthesize nanoparticles with controllable size and surface morphological features. To lower the sintering temperature with less time, spark plasma sintering is performed for bulk polycrystalline materials. SPS can also overturn the grain growth through rapid heating and low-temperature sintering, which is very prominent in retaining the morphology. Remarkably, the solid-state reaction consolidated sintering is also used to create a polycrystalline structure. In general, thermoelectric

materials are mainly fabricated through improved processes of powder metallurgy, in which a fine-grained microstructure with regulated nanostructure can be effortlessly obtained. It has been observed that hot extrusion is an effective commercial synthesis strategy that can be used to enhance the thermoelectric properties of the materials. However, further investigations are still needed to advance processes leading to an increase in the thermoelectric figure of merit of materials suitable for mass production. There is a need for body energy harvesters for power-generating wearables, which demands further investigation and development to make this a feasible technology.

Wearable devices are powered by body energy, reducing the global environmental effect of batteries and saving millions of dollars per year. The prediction of the broad market suggests replacing such devices over the current ones to avoid the need for repeated charging of wearable instruments. TEGs are considered to be passive harvesters, as there is no requirement for any action by the wearer. A lightweight and tiny integrated TEG can provide continuous and long-lasting monitoring authenticity. These TEG instruments can be introduced to the market mainly due to their durability, reliability, low cost, and eco-friendly nature by suitable modifications.

**Acknowledgments** Ganesh Shridhar Hegde (GSH) would like to acknowledge the Manipal Academy of Higher Education for providing financial support from Dr. T. M. A. doctoral fellowship. GSH would like to express special gratitude to Mr. Manoj for designing the illustrations. Additionally, GSH would like to express profound thanks towards Mr. Shrihari Rao and Mr. Ganesh Krishna for their cooperation.

**Author Contributions** ANP: Idea of the review article, supervision, validation, correction. GSH: Literature survey and analysis, writing first draft.

**Funding** Open access funding provided by Manipal Academy of Higher Education, Manipal.

**Conflict of interest** All authors certify that they have no affiliations with or involvement in any organization or entity with any financial interest or nonfinancial interest in the subject matter or materials discussed in this manuscript declaration of interest.

**Open Access** This article is licensed under a Creative Commons Attribution 4.0 International License, which permits use, sharing, adaptation, distribution and reproduction in any medium or format, as long as you give appropriate credit to the original author(s) and the source, provide a link to the Creative Commons licence, and indicate if changes were made. The images or other third party material in this article are included in the article's Creative Commons licence, unless indicated otherwise in a credit line to the material. If material is not included in the article's Creative Commons licence and your intended use is not permitted by statutory regulation or exceeds the permitted use, you will need to obtain permission directly from the copyright holder. To view a copy of this licence, visit <http://creativecommons.org/licenses/by/4.0/>.

## References

1. F.J. DiSalvo, Thermoelectric cooling and power generation. *Science (80-)* 285, 703 (1999).
2. L.E. Bell, Cooling, heating, generating power, and recovering waste heat with thermoelectric systems. *Science (80-)* 321, 1457 (2008).
3. H. Qing, W. Lijian, Z. Qian, L. Chang, D. Dongmei, and L. Wenyi, Thermodynamic analysis and optimization of liquefied air energy storage system. *Energy* 173, 162 (2019).
4. J.P. Heremans, R.J. Cava, and N. Samarth, Tetradymites as thermoelectrics and topological insulators. *Nat. Rev. Mater.* 2, 17049 (2017).
5. Z. Qi-Hao, X. Lei-Lei, W. Lian-Jun, and J. Wan, Effects of different amount of Se-doping on microstructures and thermoelectric properties of n-type  $\text{Bi}_2\text{Te}_{3-x}\text{Se}_x$ . *J. Inorg. Mater.* 29, 1139 (2014).
6. Y. Tang, Z.M. Gibbs, L.A. Agapito, G. Li, H.-S. Kim, M.B. Nardelli, S. Curtarolo, and G.J. Snyder, Convergence of multi-valley bands as the electronic origin of high thermoelectric performance in  $\text{CoSb}_3$  skutterudites. *Nat. Mater.* 14, 1223 (2015).
7. S. Wang, J. Yang, L. Wu, P. Wei, W. Zhang, and J. Yang, On Intensifying carrier impurity scattering to enhance thermoelectric performance in Cr-doped  $\text{CeyCo}_4\text{Sb}_{12}$ . *Adv. Funct. Mater.* 25, 6660 (2015).
8. T. Zhu, C. Fu, H. Xie, Y. Liu, and X. Zhao, High efficiency half-Heusler thermoelectric materials for energy harvesting. *Adv. Energy Mater.* 5, 1500588 (2015).
9. C. Fu, S. Bai, Y. Liu, Y. Tang, L. Chen, X. Zhao, and T. Zhu, Realizing high figure of merit in heavy-band p-type half-Heusler thermoelectric materials. *Nat. Commun.* 6, 8144 (2015).
10. D.Y. Chung, T. Hogan, P. Brazis, M. Rocci-Lane, C. Kannewurf, M. Bastea, C. Uher, and M.G. Kanatzidis, A new thermoelectric material:  $\text{CsBi}_4\text{Te}_6$ . *Science (80-)* 287, 1024 (2000).
11. X. Shi, J. Yang, S. Bai, J. Yang, H. Wang, M. Chi, J.R. Salvador, W. Zhang, L. Chen, and W. Wong-Ng, Multiple-filled skutterudites: high thermoelectric figure of merit through separately optimizing electrical and thermal transports. *Adv. Funct. Mater.* 20, 755 (2010).
12. L.-D. Zhao, S.-H. Lo, Y. Zhang, H. Sun, G. Tan, C. Uher, C. Wolverton, V.P. Dravid, and M.G. Kanatzidis, Ultralow thermal conductivity and high thermoelectric figure of merit in  $\text{SnSe}$  crystals. *Nature* 508, 373 (2014).
13. A.T. Duong, V.Q. Nguyen, G. Duvjir, V.T. Duong, S. Kwon, J.Y. Song, J.K. Lee, J.E. Lee, S. Park, T. Min, J. Lee, J. Kim, and S. Cho, Achieving  $ZT = 2.2$  with Bi-doped n-type  $\text{SnSe}$  single crystals. *Nat. Commun.* 7, 13713 (2016).
14. L.-D. Zhao, G. Tan, S. Hao, J. He, Y. Pei, H. Chi, H. Wang, S. Gong, H. Xu, V.P. Dravid, C. Uher, G.J. Snyder, C. Wolverton, and M.G. Kanatzidis, Ultrahigh power factor and thermoelectric performance in hole-doped single-crystal  $\text{SnSe}$ . *Science (80-)* 351, 141 (2016).
15. K. Peng, X. Lu, H. Zhan, S. Hui, X. Tang, G. Wang, J. Dai, C. Uher, G. Wang, and X. Zhou, Broad temperature plateau for high  $ZT$  s in heavily doped p-type  $\text{SnSe}$  single crystals. *Energy Environ. Sci.* 9, 454 (2016).
16. N. Toshima, Conductive polymers as a new type of thermoelectric material. *Macromol. Symp.* 186, 81 (2002).
17. K. Biswas, J. He, I.D. Blum, C.-I. Wu, T.P. Hogan, D.N. Seidman, V.P. Dravid, and M.G. Kanatzidis, High-performance bulk thermoelectrics with all-scale hierarchical architectures. *Nature* 489, 414 (2012).

18. Y. Pei, X. Shi, A. LaLonde, H. Wang, L. Chen, and G.J. Snyder, Convergence of electronic bands for high performance bulk thermoelectrics. *Nature* 473, 66 (2011).
19. D. James, X. Lu, A.C. Nguyen, D. Morelli, and S.L. Brock, Design of lead telluride based thermoelectric materials through incorporation of lead sulfide inclusions or ligand stripping of nanosized building blocks. *J. Phys. Chem. C* 119, 4635 (2015).
20. H. Shi, D. Parker, M.-H. Du, and D.J. Singh, Prospective high thermoelectric performance of the heavily p-doped half-Heusler compound CoVSn. *Phys. Rev. Appl.* 3, 014004 (2015).
21. J.J. Gong, A.J. Hong, J. Shuai, L. Li, Z.B. Yan, Z.F. Ren, and J.-M. Liu, Investigation of the bipolar effect in the thermoelectric material CaMgBi<sub>2</sub> using a first-principles study. *Phys. Chem. Chem. Phys.* 18, 16566 (2016).
22. H. Wang, A.D. Lalonde, Y. Pei, and G.J. Snyder, The criteria for beneficial disorder in thermoelectric solid solutions. *Adv. Funct. Mater.* 23, 1586 (2013).
23. D.L. Greenaway and G. Harbeke, Band structure of bismuth telluride, bismuth selenide and their respective alloys. *J. Phys. Chem. Solids* 26, 1585 (1965).
24. S. Augustine and E. Mathai, Effects of fast electron bombardment and annealing on Bi<sub>2</sub>Te<sub>3</sub> and Bi<sub>2</sub>Te<sub>2.9</sub>Se<sub>0.1</sub> single crystals. *Semicond. Sci. Technol.* 18, 745 (2003).
25. P.G. Klemens, The scattering of low-frequency lattice waves by static imperfections. *Proc. Phys. Soc. Sect. A* 68, 1113 (1955).
26. K. Zhao, A.B. Blichfeld, H. Chen, Q. Song, T. Zhang, C. Zhu, D. Ren, R. Hanus, P. Qiu, B.B. Iversen, F. Xu, G.J. Snyder, X. Shi, and L. Chen, Enhanced thermoelectric performance through tuning bonding energy in Cu<sub>2</sub>Se<sub>1-x</sub>S<sub>x</sub> liquid-like materials. *Chem. Mater.* 29, 6367 (2017).
27. F.D. Rosi, B. Abeles, and R.V. Jensen, Materials for thermoelectric refrigeration. *J. Phys. Chem. Solids* 10, 191 (1959).
28. D.M. Rowe, *Thermoelectrics to Nano* (CRC Press, 2010).
29. H.J. Goldsmid, Bismuth telluride and its alloys as materials for thermoelectric generation. *Materials (Basel)* 7, 2577 (2014).
30. H.S. Kim, S. Il-Kim, K.H. Lee, S.W. Kim, and G.J. Snyder, Phonon scattering by dislocations at grain boundaries in polycrystalline Bi<sub>0.5</sub>Sb<sub>1.5</sub>Te<sup>3</sup>. *Phys. Status Solidi Basic Res.* 254, 1 (2017).
31. M. Gradhand, M. Czerner, D.V. Fedorov, P. Zahn, B.Y. Yavorsky, L. Szunyogh, and I. Mertig, Spin polarization on Fermi surfaces of metals by the KKR method. *Phys. Rev. B* 80, 224413 (2009).
32. G.S. Hegde, A.N. Prabhu, and M.K. Chattopadhyay, Improved electrical conductivity and power factor in Sn and Se co-doped melt-grown Bi<sub>2</sub>Te<sub>3</sub> single crystal. *J. Mater. Sci. Mater. Electron.* 32, 24871 (2021).
33. Z. Ding, S.-C. Huang, D. Marcus, and R.B. Kaner, in *Eighteenth Int. Conf. Thermoelectr. Proceedings, ICT'99* (Cat. No. 99TH8407) (IEEE, n.d.), pp. 721–724.
34. J.P. Heremans, The ugly duckling. *Nature* 508, 327 (2014).
35. G.S. Hegde, A.N. Prabhu, C.F. Yang, and Y.K. Kuo, Reduction in electrical resistivity of bismuth selenide single crystal via Sn and Te co-doping. *Mater. Chem. Phys.* 278, 125675 (2021).
36. J.H. Son, M.W. Oh, B.S. Kim, S.D. Park, B.K. Min, M.H. Kim, and H.W. Lee, Effect of ball milling time on the thermoelectric properties of p-type (Bi, Sb)<sub>2</sub>Te<sub>3</sub>. *J. Alloys Compd.* 566, 168 (2013).
37. J. Horák, K. Čermák, and L. Koudelka, Energy formation of antisite defects in doped Sb<sub>2</sub>Te<sub>3</sub> and Bi<sub>2</sub>Te<sub>3</sub> crystals. *J. Phys. Chem. Solids* 47, 805 (1986).
38. A. Manabe, A. Mitsuiishi, and H. Yoshinaga, Infrared lattice reflection spectra of II–VI compounds. *Jpn. J. Appl. Phys.* 6, 593 (1967).
39. N. Jaziri, A. Boughamoura, J. Müller, B. Mezghani, F. Tounsi, and M. Ismail, A comprehensive review of thermoelectric generators: technologies and common applications. *Energy Rep.* 6, 264 (2020).
40. Q. Zhang, B. Gu, Y. Wu, T. Zhu, T. Fang, Y. Yang, J. Liu, B. Ye, and X. Zhao, Evolution of the intrinsic point defects in bismuth telluride-based thermoelectric materials. *ACS Appl. Mater. Interfaces* 11, 41424 (2019).
41. D. Enescu ed., *Thermoelectric Energy Harvesting: Basic Principles and Applications, Green Energy Advances*. (IntechOpen, 2019).
42. M.R. Sarker, A. Mohamed, and R. Mohamed, Review on comparison of different energy storage technologies used in micro-energy harvesting, WSNs, low-cost microelectronic devices: challenges and recommendations. *Appl. Mech. Mater.* 785, 131 (2015).
43. Y. Peng, K.D. Choo, S. Oh, I. Lee, T. Jang, Y. Kim, J. Lim, D. Blaauw, and D. Sylvester, An efficient piezoelectric energy harvesting interface circuit using a sense-and-set rectifier. *IEEE J. Solid State Circuits* 54, 3348 (2019).
44. R. Zybala and K.T. Wojciechowski, Anisotropy analysis of thermoelectric properties of Bi<sub>2</sub>Te<sub>2.9</sub>Se<sub>0.1</sub> prepared by SPS method. *AIP Conf. Proc.* 1449, 393 (2012).
45. J.R. Sootsman, D.Y. Chung, and M.G. Kanatzidis, New and old concepts in thermoelectric materials. *Angew. Chem. Int. Ed.* 48, 8616 (2009).
46. A. Zevalkink, D.M. Sniadak, J.L. Blackburn, A.J. Ferguson, M.L. Chabinyk, O. Delaire, J. Wang, K. Kovnir, J. Martin, L.T. Schelhas, T.D. Sparks, S.D. Kang, M.T. Dylla, G.J. Snyder, B.R. Ortiz, and E.S. Toberer, A practical field guide to thermoelectrics: fundamentals, synthesis, and characterization. *Appl. Phys. Rev.* 5, 021303 (2018).
47. S. Lee, K. Esfarjani, T. Luo, J. Zhou, Z. Tian, and G. Chen, Resonant bonding leads to low lattice thermal conductivity. *Nat. Commun.* 5, 3525 (2014).
48. O. Caha, A. Dubroka, J. Humlíček, V. Holý, H. Steiner, M. Ul-Hassan, J. Sánchez-Barriga, O. Rader, T.N. Stanislavchuk, A.A. Sirenko, G. Bauer, and G. Springholz, Growth, structure, and electronic properties of epitaxial bismuth telluride topological insulator films on BaF<sub>2</sub> (111) substrates. *Cryst Growth Des.* 13, 3365 (2013).
49. I.T. Witting, J.A. Grovogui, V.P. Dravid, and G.J. Snyder, Thermoelectric transport enhancement of Te-rich bismuth antimony telluride (Bi<sub>0.5</sub>Sb<sub>1.5</sub>Te<sub>3+x</sub>) through controlled porosity. *J. Mater.* 6, 532 (2020).
50. G.S. Hegde, A.N. Prabhu, A. Rao, and P.D. Babu, Enhancement of thermoelectric performance of In doped Bi<sub>2</sub>Te<sub>2.7</sub>Se<sub>0.3</sub> compounds. *Phys B Condens. Matter* 584, 412087 (2020).
51. G.S. Hegde, A.N. Prabhu, R.Y. Huang, and Y.K. Kuo, Reduction in thermal conductivity and electrical resistivity of indium and tellurium co-doped bismuth selenide thermoelectric system. *J. Mater. Sci. Mater. Electron.* 31, 19511 (2020).
52. S. Bano, M.V.G. Padmavati, A. Singh, M. Gandhi, M. Upadhyay, S.R. Dhakate, and D.K. Misra, Role of excess Te in Bi<sub>0.5</sub>Sb<sub>1.5</sub>Te<sub>3+x</sub> (x = 0, 0.01, 0.015 and 0.020) on the optimization of thermoelectric properties. *Mater. Sci. Semicond. Process.* 120, 10529 (2020).
53. Y.M. Zhou, H.J. Wu, Y.L. Pei, C. Chang, Y. Xiao, X. Zhang, S.K. Gong, J.Q. He, and L.D. Zhao, Strategy to optimize the overall thermoelectric properties of SnTe via compositing with its property-counter CuInTe<sub>2</sub>. *Acta Mater.* 125, 542 (2017).
54. Y. Deng, X. Zhou, G. Wei, J. Liu, C.-W. Nan, and S. Zhao, Solvothermal preparation and characterization of nanocrystalline Bi<sub>2</sub>Te<sub>3</sub> powder with different morphology. *J. Phys. Chem. Solids* 63, 2119 (2002).
55. A. Purkayastha, S. Kim, D.D. Gandhi, P.G. Ganesan, T. Borca-Tasciuc, and G. Ramanath, Molecularly protected bismuth telluride nanoparticles: microemulsion synthesis and



- thermoelectric transport properties. *Adv. Mater.* 18, 2958 (2006).
56. I.T. Witting, T.C. Chasapis, F. Ricci, M. Peters, N.A. Heinz, G. Hautier, and G.J. Snyder, The thermoelectric properties of bismuth telluride. *Adv. Electron. Mater.* 5, 1800904 (2019).
  57. C. Suryanarayana, E. Ivanov, and V.V. Boldyrev, Mechanical alloying and milling. *Mater. Sci. Eng. A* 304, 151 (2001).
  58. J. Liu and J.F. Li, Bi<sub>2</sub>Te<sub>3</sub> and Bi<sub>2</sub>Te<sub>3</sub>/nano-SiC prepared by mechanical alloying and spark plasma sintering. *Key Eng. Mater.* 280, 397 (2007).
  59. C.-H. Kuo, C.-S. Hwang, M.-S. Jeng, W.-S. Su, Y.-W. Chou, and J.-R. Ku, Thermoelectric transport properties of bismuth telluride bulk materials fabricated by ball milling and spark plasma sintering. *J. Alloys Compd.* 496, 687 (2010).
  60. C.-J. Yao, H.-L. Zhang, and Q. Zhang, Recent progress in thermoelectric materials based on conjugated polymers. *Polymers (Basel)* 11, 107 (2019).
  61. J.A. Ning, D.G. Zhao, P. Jia, and D. Wu, Synthesis and thermoelectric properties of ZnO/Cu<sub>2</sub>SnSe<sub>3</sub> composites. *Mater. Sci. Forum* 898, 1661 (2017).
  62. T. Iwasaki and H. Yamanouchi, Ball-impact energy analysis of wet tumbling mill using a modified discrete element method considering the velocity dependence of friction coefficient. *Chem. Eng. Res. Des.* 163, 241 (2020).
  63. A. Nozariasbmarz, B. Poudel, W. Li, H.B. Kang, H. Zhu, and S. Priya, Bismuth telluride thermoelectrics with 8% module efficiency for waste heat recovery application. *IScience* 23, 101340 (2020).
  64. S. Seo, Y. Jeong, M.-W. Oh, and B. Yoo, Effect of hydrogen annealing of ball-milled Bi<sub>0.5</sub>Sb<sub>1.5</sub>Te<sub>3</sub> powders on thermoelectric properties. *J. Alloys Compd.* 706, 576 (2017).
  65. I.V. Gasenkova and T.E. Svechnikova, Structural and transport properties of Sn-doped Bi<sub>2</sub>Te<sub>3-x</sub>Se<sub>x</sub> single crystals. *Inorg. Mater.* 40, 570 (2004).
  66. S. Karamazov, J. Horák, J. Navrátil, and P. Lošťák, Characterisation of Bi<sub>2</sub>Se<sub>3</sub> crystals highly doped with Pb. *Cryst. Res. Technol.* 32, 249 (1997).
  67. F. Li, R. Zhai, Y. Wu, Z. Xu, X. Zhao, and T. Zhu, Enhanced thermoelectric performance of n-type bismuth-telluride-based alloys via In alloying and hot deformation for mid-temperature power generation. *J. Mater.* 4, 208 (2018).
  68. Z. Starý, J. Horák, M. Stordeur, and M. Stölzer, Antisite defects in Sb<sub>2-x</sub>Bi<sub>x</sub>Te<sub>3</sub> mixed crystals. *J. Phys. Chem. Solids* 49, 29 (1988).
  69. J. Navrátil, Z. Starý, and T. Plecháček, Microstructure and thermoelectric properties of hot-extruded Bi-Te-Se bulk materials. *Mater. Res. Bull.* 31, 1559 (1996).
  70. L. Hu, T. Zhu, X. Liu, and X. Zhao, High performance n-type bismuth telluride based alloys for mid-temperature power generation. *Adv. Funct. Mater.* 24, 5211 (2014).
  71. W.-S. Liu, Q. Zhang, Y. Lan, S. Chen, X. Yan, Q. Zhang, H. Wang, D. Wang, G. Chen, and Z. Ren, Thermoelectric property studies on Cu-doped n-type Cu<sub>x</sub>Bi<sub>2</sub>Te<sub>2.7</sub>Se<sub>0.3</sub> nanocomposites. *Adv. Energy Mater.* 1, 577 (2011).
  72. F. Li, J.-F. Li, L.-D. Zhao, K. Xiang, Y. Liu, B.-P. Zhang, Y.-H. Lin, C.-W. Nan, and H.-M. Zhu, Polycrystalline BiCuSeO oxide as a potential thermoelectric material. *Energy Environ. Sci.* 5, 7188 (2012).
  73. M.K. Rajpalke, M. Kumar, B. Roul, T.N. Bhat, and S.B. Krupani-dhi, Temperature dependent electrical transport behavior of InN/GaN heterostructure based Schottky diodes. *Phys. Status Solidi Curr. Top. Solid State Phys.* 10, 381 (2013).
  74. G. Zheng, X. Su, H. Xie, Y. Shu, T. Liang, X. She, W. Liu, Y. Yan, Q. Zhang, C. Uher, M.G. Kanatzidis, and X. Tang, High thermoelectric performance of p-BiSbTe compounds prepared by ultra-fast thermally induced reaction. *Energy Environ. Sci.* 10, 2638 (2017).
  75. Q. Lognoné and F. Gascoin, Reactivity, stability and thermoelectric properties of n-Bi<sub>2</sub>Te<sub>3</sub> doped with different copper amounts. *J. Alloys Compd.* 610, 1 (2014).
  76. S.K. Mishra and L.C. Pathak, Self-propagating high-temperature synthesis (SHS) of advanced high-temperature ceramics. *Key Eng. Mater.* 395, 15 (2008).
  77. G. Zheng, X. Su, T. Liang, Q. Lu, Y. Yan, C. Uher, and X. Tang, High thermoelectric performance of mechanically robust n-type Bi<sub>2</sub>Te<sub>3-x</sub>Se<sub>x</sub> prepared by combustion synthesis. *J. Mater. Chem. A* 3, 6603 (2015).
  78. T. Liang, X. Su, X. Tan, G. Zheng, X. She, Y. Yan, X. Tang, and C. Uher, Ultra-fast non-equilibrium synthesis and phase segregation in In<sub>x</sub>Sn<sub>1-x</sub>Te thermoelectrics by SHS-PAS processing. *J. Mater. Chem. C* 3, 8550 (2015).
  79. A. Delgado, S. Cordova, I. Lopez, D. Nemir, and E. Shafirovich, mechanically activated combustion synthesis and shockwave consolidation of magnesium silicide. *J. Alloys Compd.* 658, 422 (2016).
  80. Q. Zhang, J. He, X.B. Zhao, S.N. Zhang, T.J. Zhu, H. Yin, and T.M. Tritt, In situ synthesis and thermoelectric properties of La-doped Mg<sub>2</sub>(Si, Sn) composites. *J. Phys. D: Appl. Phys.* 41, 185103 (2008).
  81. D. Yang, X. Su, Y. Yan, T. Hu, H. Xie, J. He, C. Uher, M.G. Kanatzidis, and X. Tang, Mechanochemical synthesis of high thermoelectric performance bulk Cu<sub>2</sub>X (X = S, Se) materials. *Chem. Mater.* 28, 4628 (2016).
  82. S.K. Bux, J.-P. Fleurial, and R.B. Kaner, Nanostructured materials for thermoelectric applications. *Chem. Commun.* 46, 8311 (2010).
  83. X.H. Ji, X.B. Zhao, Y.H. Zhang, B.H. Lu, and H.L. Ni, Solvothermal synthesis and thermoelectric properties of lanthanum contained Bi-Te and Bi-Se-Te alloys. *Mater. Lett.* 59, 682 (2005).
  84. Y.Q. Cao, X.B. Zhao, T.J. Zhu, X.B. Zhang, and J.P. Tu, Syntheses and thermoelectric properties of Bi<sub>2</sub>Te<sub>3</sub>/Sb<sub>2</sub>Te<sub>3</sub> bulk nanocomposites with laminated nanostructure. *Appl. Phys. Lett.* 92, 143106 (2008).
  85. E.E. Foos, R.M. Stroud, and A.D. Berry, Synthesis and characterization of nanocrystalline bismuth telluride. *Nano Lett.* 1, 693 (2001).
  86. Y. Zhang, G. Xu, J. Mi, F. Han, Z. Wang, and C. Ge, Hydrothermal synthesis and thermoelectric properties of nanostructured Bi<sub>0.5</sub>Sb<sub>1.5</sub>Te<sub>3</sub> compounds. *Mater. Res. Bull.* 46, 760 (2011).
  87. J. Fu, S. Song, X. Zhang, F. Cao, L. Zhou, X. Li, and H. Zhang, Bi<sub>2</sub>Te<sub>3</sub> nanoplates and nanoflowers: synthesized by hydrothermal process and their enhanced thermoelectric properties. *CrystEngComm* 14, 2159 (2012).
  88. H.T. Zhang, X.G. Luo, C.H. Wang, Y.M. Xiong, S.Y. Li, and X.H. Chen, Characterization of nanocrystalline bismuth telluride (Bi<sub>2</sub>Te<sub>3</sub>) synthesized by a hydrothermal method. *J. Cryst. Growth* 265, 558 (2004).
  89. J.-L. Mi, N. Lock, T. Sun, M. Christensen, M. Søndergaard, P. Hald, H.H. Hng, J. Ma, and B.B. Iversen, Biomolecule-assisted hydrothermal synthesis and self-assembly of Bi<sub>2</sub>Te<sub>3</sub> nanostring-cluster hierarchical structure. *ACS Nano* 4, 2523 (2010).
  90. S. Yokoyama, K. Sato, M. Muramatsu, T. Yamasuge, T. Itoh, K. Motomiya, H. Takahashi, and K. Tohji, Green synthesis and formation mechanism of nanostructured Bi<sub>2</sub>Te<sub>3</sub> using ascorbic acid in aqueous solution. *Adv. Powder Technol.* 26, 789 (2015).
  91. A. Nozariasbmarz and D. Vashaee, Effect of microwave processing and glass inclusions on thermoelectric properties of P-type bismuth antimony telluride alloys for wearable applications. *Energies* 13, 4524 (2020).
  92. M. Ibáñez, Z. Luo, A. Genç, L. Piveteau, S. Ortega, D. Cadavid, O. Dobrozhan, Y. Liu, M. Nachtegaal, M. Zebarjadi, J. Arbiol,

- M.V. Kovalenko, and A. Cabot, High-performance thermoelectric nanocomposites from nanocrystal building blocks. *Nat. Commun.* 7, 10766 (2016).
93. R.J. Mehta, Y. Zhang, C. Karthik, B. Singh, R.W. Siegel, T. Borca-Tasciuc, and G. Ramanath, A new class of doped nano bulk high-figure-of-merit thermoelectrics by scalable bottom-up assembly. *Nat. Mater.* 11, 233 (2012).
  94. H.Y. Chen, X.B. Zhao, Y.F. Lu, E. Mueller, and A. Mroczek, Microstructures and thermoelectric properties of  $\text{Fe}_{0.92}\text{Mn}_{0.08}\text{Si}_x$  alloys prepared by rapid solidification and hot. *J. Appl. Phys.* 94, 6621 (2003).
  95. R. Ciriminna, A. Fidalgo, V. Pandarus, F. Béland, L.M. Ilharco, and M. Pagliaro, The sol-gel route to advanced silica-based materials and recent applications. *Chem. Rev.* 113, 6592 (2013).
  96. J. Fouineau, S. Peron, M. Nowak, M. Giraud, S. Sicard, S. Ammar-Merah, and L. Sicard, Soft chemistry synthesis route toward  $\text{Bi}_2\text{Te}_3$  hierarchical hollow spheres. *J. Nanopart. Res.* 17, 4 (2015).
  97. S. Zhang, X. Zhang, Q. Lu, P. He, T. Lin, and H. Geng, Investigation of melt-spinning speed on the property of  $\text{Yb}_{0.2}\text{Ba}_{0.1}\text{Al}_{0.1}\text{Ga}_{0.1}\text{In}_{0.1}\text{La}_{0.05}\text{Eu}_{0.05}\text{Co}_{3.75}\text{Fe}_{0.25}\text{Sb}_{12}$  skutterudites. *Mater. Lett.* 260, 126960 (2020).
  98. S.Y. Wang, W.J. Xie, H. Li, X.F. Tang, and Q.J. Zhang, Effects of cooling rate on thermoelectric properties of n-type  $\text{Bi}_2(\text{Se}_{0.4}\text{Te}_{0.6})_3$  compounds. *J. Electron. Mater.* 40, 1150 (2011).
  99. V.I. Tkatch, S.N. Denis, and O.N. Beloshov, Direct measurements of the cooling of the rates in the single roller rapid solidification technique. *Acta Mater.* 45, 2821 (1997).
  100. K. Ahmad, C. Wan, M.A. Al-Eshaikh, and A.N. Kadachi, Enhanced thermoelectric performance of  $\text{Bi}_2\text{Te}_3$  based graphene nanocomposites. *Appl. Surf. Sci.* 474, 2–8 (2018).
  101. A.H. Li, M. Shahbazi, S.H. Zhou, G.X. Wang, C. Zhang, P. Jood, G. Peleckis, Y. Du, Z.X. Cheng, X.L. Wang, and Y.K. Kuo, Electronic structure and thermoelectric properties of  $\text{Bi}_2\text{Te}_3$  crystals and graphene-doped  $\text{Bi}_2\text{Te}_3$ . *Thin Solid Films* 518, 57 (2010).
  102. T.K. Dey, Electrical conductivity, thermoelectric power and figure of merit of doped Bi-Sb tapes produced by melt spinning technique. *Pramana* 34, 243 (1990).
  103. L. Hu, H. Wu, T. Zhu, C. Fu, J. He, P. Ying, and X. Zhao, Attaining high mid-temperature performance in  $(\text{Bi}, \text{Sb})_2\text{Te}$  thermoelectric materials via synergistic optimization. *Adv. Energy Mater.* 5, 1 (2015).
  104. A. Hruban, A. Materna, W. Dalecki, G. Strzelecka, M. Piersa, E. Jurkiewicz-Wegner, R. Diduszko, M. Romaniec, and W. Orłowski, Influence of chemical composition of liquid phase and growth process on physical properties of  $\text{Bi}_2\text{Se}_3$ ,  $\text{Bi}_2\text{Te}_3$  and  $\text{Bi}_2\text{Te}_2\text{Se}$  compounds. *Acta Phys. Pol. A* 120, 950 (2011).
  105. H.-S. Kim, N.A. Heinz, Z.M. Gibbs, Y. Tang, S.D. Kang, and G.J. Snyder, High thermoelectric performance in  $(\text{Bi}_{0.25}\text{Sb}_{0.75})_2\text{Te}_3$  due to band convergence and improved by carrier concentration control. *Mater. Today* 20, 452 (2017).
  106. Z.-H. Ge, Y.-H. Ji, Y. Qiu, X. Chong, J. Feng, and J. He, Enhanced thermoelectric properties of bismuth telluride bulk achieved by telluride-spilling during the spark plasma sintering process. *Scr. Mater.* 143, 90 (2018).
  107. G. Delaizir, G. Bernard-Granger, J. Monnier, R. Grodzki, O. Kim-Hak, P.-D. Szkutnik, M. Soulier, S. Saunier, D. Goeriot, O. Rouleau, J. Simon, C. Godart, and C. Navone, A comparative study of Spark Plasma Sintering (SPS), Hot Isostatic Pressing (HIP) and microwaves sintering techniques on p-type  $\text{Bi}_2\text{Te}_3$  thermoelectric properties. *Mater. Res. Bull.* 47, 1954 (2012).
  108. J.-F. Li and J. Liu, Effect of nano-SiC dispersion on thermoelectric properties of  $\text{Bi}_2\text{Te}_3$  polycrystals. *Phys. Status Solidi* 203, 3768 (2006).
  109. S.T. Han, P. Rimal, C.H. Lee, H.-S. Kim, Y. Sohn, and S.-J. Hong, Enhanced thermoelectric cooling properties of  $\text{Bi}_2\text{Te}_{3-x}\text{Se}_x$  alloys fabricated by combining casting, milling and spark plasma sintering. *Intermetallics* 78, 42 (2016).
  110. F. Yu, J. Zhang, D. Yu, J. He, Z. Liu, B. Xu, and Y. Tian, Enhanced thermoelectric figure of merit in nanocrystalline  $\text{Bi}_2\text{Te}_3$  bulk. *J. Appl. Phys.* 105, 094303 (2009).
  111. S. Vinoth, T. Balaganapathi, B. KaniAmuthan, T. Arun, I.P. Muthuselvam, F.C. Chou, and P. Thilakan,  $\text{Bi}_2\text{Te}_3$  thin hexagonal nanoplatelets: synthesis and its characterization studies. *Phys. E Low Dimens. Syst. Nanostruct.* 92, 17 (2017).
  112. B. Se, R. Liu, X. Tan, G. Ren, Y. Liu, Z. Zhou, C. Liu, Y. Lin, and C. Nan, Enhanced thermoelectric performance of Te-doped  $\text{Bi}_2\text{Se}_{3-x}\text{Te}_x$  bulks by self-propagating high-temperature synthesis. *Curr. Comput. Aided Drug Des.* 7, 257 (2017).
  113. K. Wu, Y. Yan, J. Zhang, Y. Mao, H. Xie, J. Yang, Q. Zhang, C. Uher, and X. Tang, Preparation of n-type  $\text{Bi}_2\text{Te}_3$  thermoelectric materials by non-contact dispenser printing combined with selective laser melting. *Phys. Status Solidi Rapid Res. Lett.* 11, 1700067 (2017).
  114. Y.Q. Cao, T.J. Zhu, X.B. Zhao, X.B. Zhang, and J.P. Tu, Nanostructuring and improved performance of ternary Bi-Sb-Te thermoelectric materials. *Appl. Phys. A Mater. Sci. Process.* 92, 321 (2008).
  115. P. Dharmiah and S.-J. Hong, Thermoelectric properties of  $\text{Bi}_2\text{Te}_3$  nanocrystals with diverse morphologies obtained via modified hydrothermal method. *J. Electron. Mater.* 46, 3012 (2017).
  116. P. Dharmiah and S.-J. Hong, Hydrothermal method for the synthesis of  $\text{Sb}_2\text{Te}_3$ , and  $\text{Bi}_{0.5}\text{Sb}_{1.5}\text{Te}_3$  nanoplates and their thermoelectric properties. *Int. J. Appl. Ceram. Technol.* 15, 132 (2018).
  117. Z.G. Chen, G. Hana, L. Yanga, L. Cheng, and J. Zou, Effects of yttrium doping on the thermoelectric properties of  $\text{Hf}_{0.6}\text{Zr}_{0.4}\text{NiSn}_{0.98}\text{Sb}_{0.02}$  half-Heusler alloys. *Prog. Nat. Sci. Mater. Int.* 22, 535 (2012).
  118. D.G. Ebling, A. Jacquot, M. Jägler, H. Böttner, U. Kühn, and L. Kirste, Structure and thermoelectric properties of nanocomposite bismuth telluride prepared by melt spinning or by partially alloying with IV-VI compounds. *Phys. Status Solidi Rapid Res. Lett.* 1, 238 (2007).
  119. O. Meroz, N. Elkabets, and Y. Gelbstein, Enhanced thermoelectric properties of n-type  $\text{Bi}_2\text{Te}_{3-x}\text{Se}_x$  alloys following melt-spinning. *ACS Appl. Energy Mater.* 3, 2090 (2020).
  120. X. Cai, X. Fan, Z. Rong, F. Yang, Z. Gan, and G. Li, Improved thermoelectric properties of  $\text{Bi}_2\text{Te}_{3-x}\text{Se}_x$  alloys by melt spinning and resistance pressing sintering. *J. Phys. D. Appl. Phys.* 47, 115101 (2014).
  121. W. Xie, X. Tang, Y. Yan, Q. Zhang, and T.M. Tritt, Direct observation of single dopant atom in light-emitting phosphor of  $\beta\text{-SiAlON: Eu}^{2+}$ . *Appl. Phys. Lett.* 94, 1 (2009).
  122. Y.X. Chen, F. Li, W. Wang, Z. Zheng, J. Luo, P. Fan, and T. Takeuchi, Optimization of thermoelectric properties achieved in Cu doped  $\beta\text{-In}_2\text{S}_3$  bulks. *J. Alloys Compd.* 782, 641 (2019).
  123. Q. Zhang, R. Zhai, T. Fang, K. Xia, Y. Wu, F. Liu, X. Zhao, and T. Zhu, Low-cost p-type  $\text{Bi}_2\text{Te}_{2.7}\text{Se}_{0.3}$  zone-melted thermoelectric materials for solid-state refrigeration. *J. Alloys Compd.* 831, 15473 (2020).
  124. Y. Zhang, L.P. Hu, T.J. Zhu, J. Xie, and X.B. Zhao, High yield  $\text{Bi}_2\text{Te}_3$  single crystal nanosheets with uniform morphology via a solvothermal synthesis. *Cryst. Growth Des.* 13, 645 (2013).
  125. R. Zhai, Y. Wu, T.-J. Zhu, and X.-B. Zhao, Tunable optimum temperature range of high-performance zone melted bismuth-telluride-based solid solutions. *Cryst. Growth Des.* 18, 4646 (2018).
  126. G.S. Hegde, A.N. Prabhu, Y.H. Gao, Y.K. Kuo, and V.R. Reddy, Potential thermoelectric materials of indium and

- tellurium co-doped bismuth selenide single crystals grown by melt growth technique. *J. Alloys Compd.* 866, 158814 (2021).
127. G.S. Hegde, A.N. Prabhu, A. Rao, and M.K. Chattopadhyay, Enhancement in thermoelectric figure of merit of bismuth telluride system due to tin and selenium co-doping. *Mater. Sci. Semicond. Process.* 127, 105645 (2021).
  128. L. Han, S.H. Spangsdorf, N.V. Nong, L.T. Hung, Y.B. Zhang, H.N. Pham, Y.Z. Chen, A. Roch, L. Stepien, and N. Pryds, Effects of spark plasma sintering conditions on the anisotropic thermoelectric properties of bismuth antimony telluride. *RSC Adv.* 6, 59565 (2016).
  129. J. Kim, L.T. Duy, B. Ahn, and H. Seo, Pre-oxidation effects on properties of bismuth telluride thermoelectric composites compacted by spark plasma sintering. *J. Asian Ceram. Soc.* 8, 211 (2020).
  130. S.-J. Hong and B. Chun, Microstructure and thermoelectric properties of n-type 95% Bi<sub>2</sub>Te<sub>3</sub>-5% Bi<sub>2</sub>Se<sub>3</sub> alloy produced by rapid solidification and hot extrusion. *Mater. Res. Bull.* 38, 599 (2003).
  131. S.J. Jung, B. Lee, B. Kim, and S.S. Impurity-free, mechanical doping for the reproducible fabrication of the reliable n-type Bi<sub>2</sub>Te<sub>3</sub>-based thermoelectric alloys. *Acta Mater.* 150, 153 (2018).
  132. S.J. Jung, B.H. Lee, S.O. Won, S.K. Kim, H.H. Park, J.S. Kim, and S.H. Baek, Mapping thermoelectric properties of polycrystalline n-type Bi<sub>2</sub>Te<sub>3-x</sub>Se<sub>x</sub> alloys by composition and doping level. *J. Alloys Compd.* 844, 155828 (2020).
  133. A. Parbatani, E.S. Song, J. Claypoole, and B. Yu, High performance broadband bismuth telluride tetradymite topological insulator photodiode. *Nanotechnology* 30, 165201 (2019).
  134. J. Braun, L. Kaserer, J. Stajkovic, K.-H. Leitz, B. Tabernig, P. Singer, P. Leibenguth, C. Gspan, H. Kestler, and G. Leichtfried, Molybdenum and tungsten manufactured by selective laser melting: Analysis of defect structure and solidification mechanisms. *Int. J. Refract. Met. Hard Mater.* 84, 104999 (2019).
  135. M.K. Fuccillo, M.E. Charles, Y.S. Hor, S. Jia, and R.J. Cava, Low temperature thermoelectric properties of Bi<sub>2-x</sub>Sb<sub>1</sub>TeSe<sub>2</sub> crystals near the n-p crossover. *Solid State Commun.* 152, 1208 (2012).
  136. W.G. Zeier, A. Zevalkink, Z.M. Gibbs, G. Hautier, M.G. Kanatzidis, and G.J. Snyder, Thinking like a chemist: intuition in thermoelectric materials. *Angew. Chem. Int. Ed.* 55, 6826 (2016).
  137. Y. Pan and J.F. Li, Thermoelectric performance enhancement in n-type Bi<sub>2</sub>(TeSe)<sub>3</sub> alloys owing to nanoscale inhomogeneity combined with a spark plasma-textured microstructure. *NPG Asia Mater.* 8, e275 (2016).
  138. Y. Wu, R. Zhai, and T. Zhu, Enhancing room temperature thermoelectric performance of n-type polycrystalline bismuth-telluride-based alloys via Ag doping and hot deformation. *Mater. Today Phys.* 2, 62–68 (2014).
  139. A. Krishna, N. Vijayan, B. Singh, K. Thukral, and K.K. Maurya, Crystalline perfection and mechanical investigations on vertical Bridgman grown Bismuth telluride (Bi<sub>2</sub>Te<sub>3</sub>) single crystals for thermoelectric applications. *Mater. Sci. Eng. A* 657, 33 (2016).
  140. M. Hong, Z.G. Chen, and J. Zou, Fundamental and progress of Bi<sub>2</sub>Te<sub>3</sub>-based thermoelectric materials. *Chin. Phys. B* 27, 048403 (2018).
  141. Z.H. Dughaish, Lead telluride as a thermoelectric material for thermoelectric power generation. *Phys. B Condens. Matter* 322, 205 (2002).
  142. X. Yan, B. Poudel, Y. Ma, W.S. Liu, G. Joshi, H. Wang, Y. Lan, D. Wang, G. Chen, and Z.F. Ren, Experimental studies on anisotropic thermoelectric properties and structures of n-type Bi<sub>2</sub>Te<sub>2.7</sub>Se<sub>0.3</sub>. *Nano Lett.* 10, 3373 (2010).
  143. H.P. Ha, Y.J. Oh, D.B. Hyun, and E.P. Yoon, Thermoelectric properties of n-type bismuth telluride based alloys prepared by hot pressing and zone melting method. *Int. J. Soc. Mater. Eng. Resour.* 10, 130 (2002).
  144. J. Jiang, L. Chen, S. Bai, Q. Yao, and Q. Wang, Thermoelectric properties of p-type (Bi<sub>2</sub>Te<sub>3</sub>)<sub>x</sub>(Sb<sub>2</sub>Te<sub>3</sub>)<sub>1-x</sub> crystals prepared by zone melting. *J. Cryst. Growth* 277, 258 (2005).
  145. B. Zhu, X. Liu, Q. Wang, Y. Qiu, Z. Shu, Z. Guo, Y. Tong, J. Cui, M. Gu, and J. He, Realizing record high performance in n-type Bi<sub>2</sub>Te<sub>3</sub>-based thermoelectric materials. *Energy Environ. Sci.* 13, 2106 (2020).
  146. S.K. Pundir, S. Singh, and P. Jain, Spark plasma sintering effect on thermoelectric properties of nanostructured bismuth telluride synthesized by high energy ball milling. *J. Nanosci. Nanotechnol.* 20, 3902 (2020).
  147. A.A. Abdelnabi, V. Lakhian, J.R. McDermid, Y.C. Tseng, and J.S. Cotton, Enhancement of mechanical properties and thermoelectric performance of spark plasma sintered P-type bismuth telluride by powder surface oxide reduction. *J. Alloys Compd.* 858, 157657 (2021).
  148. F.M. El-Makaty, H.K. Ahmed, and K.M. Youssef, The effect of different nanofiller materials on the thermoelectric behaviour of bismuth telluride. *Mater. Des.* 209, 109974 (2021).
  149. M. Bumrungron, K. Hirota, K. Takagi, K. Hanasaku, T. Hirai, I. Morioka, R. Yasufuku, M. Kitamura, and K. Hasezaki, Synthesis and thermoelectric properties of bismuth antimony telluride thermoelectric materials fabricated at various ball-milling speeds with yttria-stabilized zirconia ceramic vessel and balls. *Ceram. Int.* 46, 13869 (2020).
  150. G. Shyam Shendur, M. Abeens, R. Muruganadhan, M. Arivanandhan, M. Premnath, and E. Rajasekaran, Investigation of nano ceramics added bismuth antimony telluride for energy harvesting applications. *Mater. Today Proc.* 22, 879 (2020).
  151. I. Terasaki, Y. Sasago, and K. Uchinokura, Large thermoelectric power in NaCo<sub>2</sub>O<sub>4</sub> single crystals. *Phys. Rev. B* 56, R12685 (1997).
  152. R. Murugasami, P. Vivekanandhan, S. Kumaran, R. Suresh Kumar, and T. John Tharakan, Simultaneous enhancement in thermoelectric performance and mechanical stability of p-type SiGe alloy doped with Boron prepared by mechanical alloying and spark plasma sintering. *J. Alloys Compd.* 773, 752 (2019).
  153. H. Wang, G. Wu, Z. Yan, X. Tan, J. Cai, H. Hu, P. Sun, G. Liu, and J. Jiang, Synergistic effects of B-In codoping in zone-melted Bi<sub>0.48</sub>Sb<sub>1.52</sub>Te<sub>3</sub>-based thermoelectric. *Chem. Eng. J.* 429, 13038 (2021).
  154. M.B. Limoei, H. Ebrahimifar, S. Hosseini, and A.A. Branch, Study of the oxidation resistance of coated AISI 441 ferritic stainless steel for SOFCs. *Int. J. Chem. Mol. Nucl. Mater. Metall. Eng.* 20, 533 (2013).
  155. A. Jacquot, J. Thomas, J. Schumann, M. Jägler, H. Böttner, T. Gemming, J. Schmidt, and D. Ebling, (Bi, Sb)<sub>2</sub>Te<sub>3</sub>-PbTe chalcogenide alloys: impact of the cooling rate and sintering parameters on the microstructures and thermoelectric performances. *J. Mater. Res.* 26, 2460 (2011).
  156. S. Ma, C. Li, P. Wei, W. Zhu, X. Nie, X. Sang, Q. Zhang, and W. Zhao, High-pressure synthesis and excellent thermoelectric performance of Ni/BiTeSe magnetic nanocomposites. *J. Mater. Chem. A* 8, 4816 (2020).
  157. D.S. Lee, T.-H. Kim, C.-H. Park, C.-Y. Chung, Y.S. Lim, W.-S. Seo, and H.-H. Park, Crystal structure, properties and nanostructuring of a new layered chalcogenide semiconductor, Bi<sub>2</sub>MnTe<sub>4</sub>. *CrystEngComm* 15, 5532 (2013).
  158. Y. Zheng, H. Xie, Q. Zhang, A. Suwardi, X. Cheng, Y. Zhang, W. Shu, X. Wan, Z. Yang, Z. Liu, and X. Tang, Unraveling the critical role of melt-spinning atmosphere in enhancing the thermoelectric performance of p-type Bi<sub>0.52</sub>Sb<sub>1.48</sub>Te<sub>3</sub> alloys. *ACS Appl. Mater. Interfaces* 12, 36186 (2020).
  159. V. Ohorodniichuk, A. Dauscher, E. Branco-Lopes, S. Migot, C. Candolfi, and B. Lenoir, Structural and electrical properties

- characterization of  $\text{Sb}_{1.52}\text{Bi}_{0.48}\text{Te}_{3.0}$  melt-spun ribbons. *Curr. Comput.-Aided Drug Des.* 7, 172 (2017).
160. C. Zhao-kun, F. Ping, Z. Zhuang-hao, L. Peng-juan, C. Tian-bao, C. Xing-min, L. Jing-ting, L. Guang-xing, and Z. Dong-ping, Thermoelectric properties and micro-structure characteristics of annealed N-type bismuth telluride thin film. *Appl. Surf. Sci.* 280, 225 (2013).
  161. H.-S. Kim, T. Kim, J. An, D. Kim, J.H. Jeon, and S. Kim, Segregation of  $\text{NiTe}_2$  and  $\text{NbTe}_2$  in p-type thermoelectric  $\text{Bi}_{0.5}\text{Sb}_{1.5}\text{Te}_3$  alloys for carrier, energy filtering effect by melt spinning. *Appl. Sci.* 11, 910 (2021).
  162. F.F. Jaldurgam, Z. Ahmad, and F. Touati, Synthesis and performance of large-scale cost-effective environment-friendly nanostructured thermoelectric materials. *Nanomaterials* 11, 1091 (2021).
  163. J.-S. Rhyee and J. Kim, Chemical potential tuning and enhancement of thermoelectric properties in indium selenides. *Materials (Basel)* 8, 1283 (2015).
  164. O. Ivanov, M. Yaprincev, A. Vasil'ev, and E. Yaprinceva, Microstructure and thermoelectric properties of the medium-entropy block-textured  $\text{BiSbTe}_{1.5}\text{Se}_{1.5}$  alloy. *J. Alloys Compd.* 872, 159743 (2021).
  165. R. Taziwa, E. Meyer, D. Katwire, and L. Ntozakhe, Influence of carbon modification on the morphological, structural, and optical properties of zinc oxide nanoparticles synthesized by pneumatic spray pyrolysis technique. *J. Nanomater.* 2017, 1 (2017).
  166. M. Scheele, N. Oeschler, K. Meier, A. Kornowski, C. Klinker, and H. Weller, Synthesis and thermoelectric characterization of  $\text{Bi}_2\text{Te}_3$  nanoparticles. *Adv. Funct. Mater.* 19, 3476 (2009).
  167. F. Wu, H. Song, J. Jia, and X. Hu, Effects of Ce, Y, and Sm doping on the thermoelectric properties of  $\text{Bi}_2\text{Te}_3$  alloy. *Prog. Nat. Sci. Mater. Int.* 23, 408 (2013).
  168. Y.H. Zhang, T.J. Zhu, J.P. Tu, and X.B. Zhao, Flower-like nanostructure and thermoelectric properties of hydrothermally synthesized La-containing  $\text{Bi}_2\text{Te}_3$  based alloys. *Mater. Chem. Phys.* 103, 484 (2007).
  169. W. Guo, J. Ma, and W. Zheng,  $\text{Bi}_2\text{Te}_3$  nanoflowers assembled of defective nanosheets with enhanced thermoelectric performance. *J. Alloys Compd.* 659, 177 (2016).
  170. C. Hollar, Z. Lin, M. Kongara, T. Varghese, C. Karthik, J. Schimpf, and J. Eixenberger, High-performance flexible bismuth telluride thin film from solution processed colloidal nanoplates. *Adv. Mater. Technol.* 5, 2000600 (2020).
  171. Z.J. Vafa, M. Mehdi, and B. Mohagheghi, Synthesis of high purity bismuth telluride ( $\text{Bi}_2\text{Te}_3$ ) nanostructures by co-precipitation process and annealing under hydrazine vapor: structural and thermoelectric studies. *J. Electron. Mater.* 4, 14 (2021).
  172. S.K. Kanta, S. Paul, T. Chatterjee, H. Dutta, and S.K. Pradhan, Microstructure and electrical characterization of thermoelectric nanocrystalline  $\text{Bi}_2\text{Te}_3$  synthesized by mechanical alloying. *Mater. Res.* 22, 1 (2019).
  173. F. Suarez, A. Nozariasmarz, D. Vashae, and M.C. Öztürk, Designing thermoelectric generators for self-powered wearable electronics. *Energy Environ. Sci.* 9, 2099 (2016).
  174. B. Hamawandi, H. Mansouri, S. Ballikaya, Y. Demirci, M. Orlovská, N. Bolghanabadi, S.A. Sajjadi, and M.S. Toprak, A comparative study on the thermoelectric properties of bismuth chalcogenide alloys synthesized through mechanochemical alloying and microwave-assisted solution synthesis routes. *Front. Mater.* 7, 332 (2020).
  175. B. Zhou, Y. Zhao, L. Pu, and J.-J. Zhu, Microwave-assisted synthesis of nanocrystalline  $\text{Bi}_2\text{Te}_3$ . *Mater. Chem. Phys.* 96, 192 (2006).
  176. A.A. Abdelnabi, V. Lakhian, and J.R. McDermid, The effect of powder pre-treatment on the mechanical and thermoelectric properties of spark plasma sintered N-type bismuth telluride. *J. Alloys Compd.* 874, 159782 (2021).
  177. N.S. Chauhan, O.I. Lebedev, K. Kovnir, S.V. Pyrlin, L.S.A. Marques, M.M.D. Ramos, B.A. Korgel, and Y.V. Kolen'ko, Scalable colloidal synthesis of  $\text{Bi}_2\text{Te}_{2.7}\text{Se}_{0.3}$  plate-like particles give access to a high-performing n-type thermoelectric material for low temperature application. *Nanoscale Adv.* 2, 5699 (2020).
  178. Y. Du, J. Xua, B. Paul, and P. Eklund, Flexible thermoelectric materials and devices. *Appl. Mater. Today* 16, 13 (2015).
  179. B. Hamawandi, H. Batili, M. Paul, S. Ballikaya, N.I. Kilic, R. Szukiewicz, M. Kuchowicz, M. Johnsson, and M.S. Toprak, Minute-made, high-efficiency nanostructured  $\text{Bi}_2\text{Te}_3$  via High-throughput, green solution chemical synthesis. *Nanomaterials* 4, 2053 (2021).
  180. S.S. Lim, K.-C. Kim, H. Jeon, J. Kim, J. Kang, H. Park, S. Baek, J. Kim, and S. Keun Kim, Enhanced thermal stability of  $\text{Bi}_2\text{Te}_3$ -based alloys via interface engineering with atomic layer deposition. *J. Eur. Ceram. Soc.* 40, 3592 (2020).
  181. J.M. Schultz, J.P. McHugh, and W.A. Tiller, Effects of heavy deformation and annealing on the electrical properties of  $\text{Bi}_2\text{Te}_3$ . *J. Appl. Phys.* 12, 366 (2018).
  182. J.R. Drabble, R.D. Groves, and R. Wolfe, Galvanomagnetic effects in n-type bismuth telluride. *Proc. Phys. Soc.* 71, 430 (1958).
  183. N. Narendra, P. Norouzzadeh, D. Vashae, and K.W. Kim, Doping induced enhanced density of states in bismuth telluride. *Appl. Phys. Lett.* 111, 232101 (2017).
  184. B. Wiendlocha, Resonant levels, vacancies, and doping in  $\text{Bi}_2\text{Te}_3$ ,  $\text{Bi}_2\text{Te}_2\text{Se}$ , and  $\text{Bi}_2\text{Se}_3$  tetradymites. *J. Electron. Mater.* 45, 3515 (2016).
  185. Q. Zhang, B. Liao, Y. Lan, K. Lukas, W. Liu, K. Esfarjani, C. Opeil, D. Broido, G. Chen, and Z. Ren, High thermoelectric performance by resonant dopant indium in nanostructured  $\text{SnTe}$ . *Proc. Natl. Acad. Sci. USA* 110, 13261 (2013).
  186. C.M. Jaworski, B. Wiendlocha, V. Jovic, and J.P. Heremans, Combining alloy scattering of phonons and resonant electronic levels to reach a high thermoelectric figure of merit in  $\text{PbTeSe}$  and  $\text{PbTeS}$  alloys. *Energy Environ. Sci.* 4, 4155 (2011).
  187. A. Datta, J. Paul, A. Kar, A. Patra, Z. Sun, L. Chen, J. Martin, and G.S. Nolas, Facile chemical synthesis of nanocrystalline thermoelectric alloys based on Bi-Sb-Te-Se. *Cryst. Growth Des.* 10, 3983 (2010).
  188. G.S. Nolas, J. Yang, and H.J. Goldsmid, *Therm. Conduct.* (Springer US, n.d.), pp. 123–152.
  189. H.J. Goldsmid, A.R. Sheard, and D.A. Wright, The performance of bismuth telluride thermojunctions. *Br. J. Appl. Phys.* 9, 365 (1958).
  190. A. Aresti, A. Congiu, P. Manca, and A. Spiga, Thermal conductivity of  $\text{CdS}_x\text{Se}_{1-x}$  solid solutions. *J. Appl. Phys.* 44, 3401 (1973).
  191. W.M. Yim and F.D. Rosi, Compound tellurides and their alloys for peltier cooling—a review. *Solid State. Electron.* 15, 1121 (1972).
  192. B. Saggini, M. Tarabini, and G. Lanfranchi, A device for the skin-contact thermal resistance measurement. *IEEE Trans. Instrum. Meas.* 61, 489 (2012).
  193. H.J. Wu, L.-D. Zhao, F.S. Zheng, D. Wu, Y.L. Pei, X. Tong, M.G. Kanatzidis, and J.Q. He, Broad temperature plateau for thermoelectric figure of merit  $ZT > 2$  in phase-separated  $\text{PbTe}_{0.7}\text{S}_{0.3}$ . *Nat. Commun.* 5, 4515 (2014).
  194. S. Riffat and X. Ma, Thermoelectrics: a review of present and potential applications. *Appl. Therm. Eng.* 23, 913 (2003).
  195. L.A. Kuznetsova, V.L. Kuznetsov, and D.M. Rowe, Thermoelectric properties and crystal structure of ternary compounds in the Ge (Sn, Pb) Te- $\text{Bi}_2\text{Te}_3$  systems. *J. Phys. Chem. Solids* 61, 1269 (2000).

196. T. Kuroki, K. Kabeya, K. Makino, T. Kajihara, H. Kaibe, H. Hachiuma, H. Matsuno, and A. Fujibayashi, Thermoelectric generation using waste heat in steel works. *J. Electron. Mater.* 43, 2405 (2014).
197. E.M.F. Vieira, A.L. Pires, J.P.B. Silva, V.H. Magalhães, J. Grilo, F.P. Brito, M.F. Silva, A.M. Pereira, and L.M. Gonçalves, High-performance  $\mu$ -thermoelectric device based on  $\text{Bi}_2\text{Te}_3/\text{Sb}_2\text{Te}_3$  p-n junctions. *ACS Appl. Mater. Interfaces* 11, 38946 (2019).
198. F. Invernizzi, S. Dulio, M. Patrini, G. Guizzetti, and P. Mustarelli, Energy harvesting from human motion: materials and techniques. *Chem. Soc. Rev.* 45, 5455 (2016).
199. S. Dalola, M. Ferrari, V. Ferrari, M. Guizzetti, D. Marioli, and A. Taroni, Characterization of thermoelectric modules for powering autonomous sensors. *IEEE Trans. Instrum. Meas.* 58, 99 (2009).
200. V. Leonov and R.J.M. Vullers, Wearable thermoelectric generators for body-powered devices. *J. Electron. Mater.* 38, 1491 (2009).
201. V. Leonov and R.J.M. Vullers, Wearable electronics self-powered by using human body heat: the state of the art and the perspective. *J. Renew. Sustain. Energy* 1, 062701 (2009).
202. B. Poudel, Q. Hao, Y. Ma, Y. Lan, A. Minnich, B. Yu, X. Yan, D. Wang, A. Muto, D. Vashaee, X. Chen, J. Liu, M.S. Dresselhaus, G. Chen, and Z. Ren, High-thermoelectric performance of nanostructured bismuth antimony telluride bulk alloys. *Science* (80-) 320, 634 (2008).
203. A. Lawal, A. Shaari, R. Ahmed, M.H. Ali, and N. Jarkoni, Electronic and optical properties of  $\text{Bi}_2\text{Se}_3$  topological insulator: a promising absorbing layer for broadband photodetector. *ARPJ. Eng. Appl. Sci.* 12, 5880 (2017).
204. M. Hyland, H. Hunter, J. Liu, E. Veety, and D. Vashaee, Wearable thermoelectric generators for human body heat harvesting. *Appl. Energy* 182, 518 (2016).
205. A. Nozariasbmarz, H. Collins, K. Dsouza, M.H. Polash, M. Hosseini, M. Hyland, J. Liu, A. Malhotra, F.M. Ortiz, F. Mohaddes, V.P. Ramesh, Y. Sargolzaeiaval, N. Snouwaert, M.C. Öztürk, and D. Vashaee, Review of wearable thermoelectric energy harvesting: from body temperature to electronic systems. *Appl. Energy* 258, 114069 (2020).
206. G. Chen, M.S. Dresselhaus, G. Dresselhaus, J.-P. Fleurial, and T. Caillat, Recent developments in thermoelectric materials. *Int. Mater. Rev.* 48, 45 (2003).
207. S. Li, H.M.A. Soliman, J. Zhou, M.S. Toprak, M. Muhammed, D. Platzek, P. Ziolkowski, and E. Müller, Effects of annealing and doping on nanostructured bismuth telluride thick films. *Chem. Mater.* 20, 4403 (2008).
208. D.K. Aswal, R. Basu, and A. Singh, Key issues in development of thermoelectric power generators: High figure-of-merit materials and their highly conducting interfaces with metallic interconnects. *Energy Convers. Manag.* 114, 50 (2016).
209. J. Sharp, J. Bierschen, and H.B. Lyon, Overview of solid-state thermoelectric refrigerators and possible applications to on-chip thermal management. *Proc. IEEE* 94, 1602 (2006).
210. X.Y. Huang, Z. Xu, and L.D. Chen, The thermoelectric performance of  $\text{ZrNiSn}/\text{ZrO}_2$  composites. *Solid State Commun.* 130, 181 (2004).
211. W. Xie, X. Tang, Y. Yan, Q. Zhang, and T.M. Tritt, High thermoelectric performance  $\text{BiSbTe}$  alloy with unique low-dimensional structure. *J. Appl. Phys.* 105, 113713 (2009).
212. V. Leonov, Thermoelectric energy harvesting of human body heat for wearable sensors. *IEEE Sens. J.* 13, 2284 (2013).
213. J.-H. Bahk, H. Fang, K. Yazawa, and A. Shakouri, Flexible thermoelectric materials and device optimization for wearable energy harvesting. *J. Mater. Chem. C* 3, 10362 (2015).
214. C.M. Kim, S.H. Kim, T. Onimaru, K. Suekuni, T. Takabatake, and M.H. Jung, Thermoelectric properties in Mn-doped  $\text{Bi}_2\text{Se}_3$ . *Curr. Appl. Phys.* 14, 1041 (2014).
215. M. Lossec, B. Multon, H. Ben Ahmed, and C. Goupil, Thermoelectric generator placed on the human body: system modeling and energy conversion improvements. *Eur. Phys. J. Appl. Phys.* 52, 11103 (2010).
216. K. Yazawa and A. Shakouri, Cost-efficiency trade-off and the design of thermoelectric power generators. *Environ. Sci. Technol.* 45, 7548 (2011).
217. C. Navone, M. Soulier, M. Plissonnier, and A.L. Seiler, Development of  $(\text{Bi}, \text{Sb})_2(\text{Te}, \text{Se})_3$ -based thermoelectric modules by a screen-printing process. *J. Electron. Mater.* 39, 1755 (2010).

**Publisher's Note** Springer Nature remains neutral with regard to jurisdictional claims in published maps and institutional affiliations.

## Authors and Affiliations

Ganesh Shridhar Hegde<sup>1</sup> · A. N. Prabhu<sup>1</sup> 

<sup>1</sup> Department of Physics, Manipal Institute of Technology, Manipal Academy of Higher Education, Manipal 576104, India